Article

Risk Assessment of Rising Temperatures Using Landsat 4–9 LST Time Series and Meta® Population Dataset: An Application in Aosta Valley, NW Italy

Tommaso Orusa [1,2,3,*], Annalisa Viani [4], Boineelo Moyo [5,6], Duke Cammareri [2,3] and Enrico Borgogno-Mondino [1]

1   Department of Agricultural, Forest and Food Sciences (DISAFA), GEO4Agri DISAFA Lab, Università degli Studi di Torino, Largo Paolo Braccini 2, 10095 Grugliasco, Italy; enrico.borgogno@unito.it
2   Earth Observation Valle d'Aosta—eoVdA, Località L'Île-Blonde, 5, 11020 Brissogne, Italy; dcammareri@invallee.it
3   IN.VA spa, Località L'Île-Blonde, 5, 11020 Brissogne, Italy
4   Istituto Zooprofilattico Sperimentale Piemonte, Liguria e Valle d'Aosta (IZS PLV) S.C Valle d'Aosta—CeRMAS (National Reference Center for Wildlife Diseases), Località Amerique, 7/G, 11020 Quart, Italy; annalisa.viani@izsto.it
5   Department of Geoinformatics, Stuttgart University of Applied Sciences, Schellingstraße 24, 70174 Stuttgart, Germany
6   HRSL, Core Science, Meta Research, 1 Hacker Way, Menlo Park, CA 94025, USA
*   Correspondence: tommaso.orusa@unito.it

Abstract: Earth observation data have assumed a key role in environmental monitoring, as well as in risk assessment. Rising temperatures and consequently heat waves due to ongoing climate change represent an important risk considering the population, as well as animals, exposed. This study was focused on the Aosta Valley Region in NW Italy. To assess population exposure to these patterns, the following datasets have been considered: (1) HDX Meta population dataset refined and updated in order to map population distribution and its features; (2) Landsat collection (missions 4 to 9) from 1984 to 2022 obtained and calibrated in Google Earth Engine to model LST trends. A pixel-based analysis was performed considering Aosta Valley settlements and relative population distribution according to the Meta population dataset. From Landsat data, LST trends were modelled. The LST gains computed were used to produce risk exposure maps considering the population distribution and structure (such as ages, gender, etc.). To check the consistency and quality of the HDX population dataset, MAE was computed considering the ISTAT population dataset at the municipality level. Exposure-risk maps were finally realized adopting two different approaches. The first one considers only LST gain maximum by performing an ISODATA unsupervised classification clustering in which the separability of each class obtained and was checked by computing the Jeffries–Matusita (J-M) distances. The second one was to map the rising temperature exposure by developing and performing a risk geo-analysis. In this last case the input parameters considered were defined after performing a multivariate regression in which LST maximum was correlated and tested considering (a) Fractional Vegetation Cover (FVC), (b) Quote, (c) Slope, (d) Aspect, (e) Potential Incoming Solar Radiation (mean sunlight duration in the meteorological summer season), and (f) LST gain mean. Results show a steeper increase in LST maximum trend, especially in the bottom valley municipalities, and especially in new built-up areas, where more than 60% of the Aosta Valley population and domestic animals live and where a high exposure has been detected and mapped with both approaches performed. Maps produced may help the local planners and the civil protection services to face global warming from a One Health perspective.

Keywords: Google Earth Engine; USGS NASA Landsat 4–9 missions; LST timeseries analysis; risk population assessment; HDX meta population; trends modeling; Aosta Valley; Italy; Alps; climate change

1. Introduction

Temperature and summer heatwave monitoring due to ongoing climate change has assumed a crucial role in the last years worldwide [1–3]. Although studies on extreme events are increasing, and in particular on heatwaves and urban heat islands [4–8], few focus on time series derived from free Earth observation images [4,9–15]. Furthermore, there is still a lack regarding scientific and technical studies that focus on land surface temperature (hereinafter called LST) climatic trends through an analysis of the exposed population and related risks [16–18].

Nowadays, many studies focus on LST and epidemiological relationships but do not concern themselves with spatial population exposure [19–21] or animals, including wildlife [22].

1.1. Earth Observation (EO) Data Role in the Climate Change Framework

The evaluation of exposure to ambient temperatures in epidemiological studies has generally been based on records from meteorological stations which may not adequately represent local temperature variability [23].

To go beyond this limiting factor, Earth observation images represent a possible solution to carefully map environmental conditions at the local scale [20,24]. The health sector and civil protection services in recent years at the European, Italian, and local levels are particularly interested in having cartographic products and GIS to assess the risks and effects of extreme temperatures on the population by identifying the most vulnerable areas [19]. The identification of these areas would make it possible to direct territorial planning towards greening policies or measures aimed at mitigating warming and at the same time implementing forms of adaptation (for example, creation of emergency response hubs in the case of an area with a vulnerable population such as the elderly). Although free thermal data are increasing by offering medium-high spatial resolution (such as Landsat missions [25,26] with a resampled GSD of 30 m or ECOSTRESS with 60 m GSD [27–32], their use for the development of various services and applications is still limited [33–36] and therefore, offer numerous exploitation possibilities when combined with new databases made available by various governmental or research bodies.

Thermal data are widely applied nowadays to map LST and urban heat island phenomena [8,37–41]. However, their use is often confined to analysis at given moments and not in timeseries due to the need to calibrate them [34,42]. Platforms such as Google Earth Engine [43] in the case of Landsat data allow, thanks to the algorithm developed by Ermida [36], to quickly calibrate the thermal data allowing analysis on historical series.

1.2. Population Datasets

In recent years, datasets on the spatial and temporal distribution of the global population have been developed [44–46]. Nevertheless, they still have a coarse resolution. One of the most detailed is provided by the World Bank with the World Population dataset with a spatial resolution of 1 km and another of 100 m. This last is spatially coeval with the native geometric resolution for the thermal bands of the Landsat missions [46]. This dataset contains a top-down constrained breakdown of estimated population by age and gender groups from 2000 to the present year [45]. Top-down constrained age/sex structure estimate datasets for individual countries for 2020 at 100 m spatial resolution with country totals adjusted to match the corresponding official United Nations population estimates have been prepared by the Population Division of the Department of Economic and Social Affairs of the United Nations Secretariat (2019 Revision of World Population Prospects). It is worth noting that WorldPop gridded datasets on population age structures, poverty, urban growth, and population dynamics are freely available. Despite the huge amount of data, this dataset still has limited application in rural contexts and outside wide urban areas due to its geometric resolution that has limited the application at regional and local levels [47–49].

Accurate information on global population distribution is crucial to many disciplines. A population and housing census is the traditional tool for deriving small-area detailed statistics on population and its spatial distribution [50,51]. However, censuses are time-consuming, and the spatial resolution is naturally set by the census enumeration areas (EA), which lack fine-grained information about the aggregation of population. The sizes of the EAs vary by many orders of magnitude from country to country, ranging from hundreds of square meters in urban areas to tens of thousands of square kilometers in low-population areas, resulting in an average spatial resolution [50] of a census unit of 33 km at a global scale. Recently, multiple higher-resolution maps of human-made built-up areas have emerged [52,53], most notably the Global Human Settlement Layer (GHSL) [54], the Global Urban Footprint (GUF) [51,55], the WorldPop project [44,56], Landscan [57,58], and Missing Maps project [59,60]. However, none provide a scalable solution with high accuracy in rural areas. Over the last decade high-resolution (sub-meter) satellite imagery has become widely available, enabling the global collection of recent and cloud-free Earth imagery. Additionally, in the last years, the surge in research on computer vision and in particular convolutional neural networks (CNNs) have enabled bulk processing of imagery in a rapid manner [50]. The combination of these methods enables the global analysis of high-resolution imagery as a promising method for detecting individual buildings; combining building estimates with available census data to produce updated and higher-resolution population maps; and offering alternative, state-of-the-art population estimates in the absence of census data. Various approaches using machine learning have been demonstrated on small areas [50], yet a method which allows global mapping has remained elusive.

Nowadays, in fact, high-resolution datasets of population density which accurately map sparsely-distributed human populations do not exist at a global scale [49,50,61]. Typically, population data are obtained using censuses and statistical modeling. More recently, methods using remotely-sensed data have emerged, capable of effectively identifying urbanized areas. Obtaining high accuracy in the estimation of population distribution in rural areas remains a very challenging task due to the simultaneous requirements of sufficient sensitivity and resolution to detect very sparse populations through remote sensing as well as reliable performance at a global scale. Meta has recently developed a computer vision method based on machine learning to create population maps from satellite imagery and phone GNSS tracking at a global scale, with a spatial sensitivity corresponding to individual buildings and suitable for global deployment. By combining these settlement data with census data, Meta has created the HDX Meta population dataset, including raster maps with ~30 m spatial resolution for 18 countries in the world [50]. HDX is a platform which lets users, for research and management purposes, access socio-economic data mostly collected by Meta through Data for Good (https://dataforgood.facebook.com/dfg, last accessed on 18 April 2023). Data for Good at Meta's program includes tools built from de-identified Meta data, as well as tools that the company develops using satellite imagery and other publicly available sources.

1.3. Remote Sensing in Climate Change Risk Assessment

There is a growing need for the assessment and reduction of climate change risk. The effects of global warming are already bringing harm to human communities and the natural world. Further temperature rises will have a devastating impact and more action on greenhouse gas emissions is urgently required. Multiple factors contribute to climate change, and multiple actions are needed to address it [8,37–41]. Especially concerning is population exposure to climate change. In fact, nowadays, EO data and more generally remote sensing may help in mapping and developing services with particular regard to climate change risk assessment involving communities at different levels. Space-borne images for civil applications have been routinely acquired since the 1980s (Landsat and SPOT), while more recently, the European Union's Copernicus program has been acquiring images. EO data can provide remotely sensed information regarding floods, forest fires, and droughts. In general, remote sensing data from space, but also from airborne or drone

platforms, can be profitably used to manage many risks, from geo-hydrological to volcanic, and from seismic to anthropogenic. Less exploited is the application and coupling of remote sensing data with GIS health data, with particular regard to the climate change framework. Remote sensing can play a key role in managing risks, leading to a new level of understanding of the complex Earth systems and planning. In recent decades, satellite-based observations and the derived geospatial products have been successfully demonstrated to be highly valuable tools in each different phase of the risk and exposure management (forecasting, planning, emergency, and post-emergency) [34,42]. For example, synthetic aperture radar (SAR) images can facilitate risk management since they are also acquired through dense cloud cover and in both night and day conditions. This ability can help during the emergency phase. Stacks of SAR data can be used to detect subtle ground deformation induced by slow movement phenomena (e.g., slow landslides, subsidence) that can dangerously evolve, involving elements of risk [62]. On the other hand, optical images are fundamental products for monitoring land cover changes induced by several hazards (e.g., fast landslides, volcanic eruptions) or thermal data to assess, for example, urban heath islands (UHIs) and their intensity or the water stress on forests and crops. These data are routinely used to map and evaluate the elements at risk scattered over wide areas. The application of a combined use of population data at higher resolution with thermal EO data in order to evaluate the exposure to rising temperature in light of climate change has been poorly explored in the scientific community. This is due to the fact that the population datasets at higher resolution are relatively new, as is the application of EO data in the domain. For the climate change adaptation regarding the civil component, the first steps are being taken.

Moreover, the One Health approach involving thermal remote-sensed time-series analysis to assess the temperature trend gain represents a novelty compared with the well-known and over-studied UHI phenomenon which is focused only on a given time and does not permit the development of strong models. The LST trends analysis modelling and its application to coupling population data represent a novelty especially in the assessment of rising temperature exposure [8].

1.4. Coupling Population and EO Data in Climate Change Adaptation and Risk Assessment

The approach developed to map population (thanks to Meta Geo for Good) combined with free thermal EO data to model rising temperature represents a first attempt of this kind. In order to map the population exposure and risk for the first time, the highest available population dataset has been used, with a native geometrical resolution (GSD—Ground Sample Distance 30 m), which is the same as Landsat's. This may enforce the applicability and coupling of these kinds of data in the planning and management of climate change risks and adaptation, suggesting new solutions [18,63]. Furthermore, mapping the exposure of population involved according to different levels of temperature (LST) gain permits greening actions and policies to be addressed, favors the identification of new medical or health centers, permits the areas that will be more subject to emergency calls to be known in advance, allows areas or zones most at risk to be redeveloped with a view to mitigation and above all adaptation, makes forecasts on access to hospitals in case of heat waves and the impact of costs on the health sector having mapped data, and evaluates the effectiveness of requalification policies and actions and its effects on heat flows and on the risk associated with the exposed population. Then, the development of new applications and services in a technological perspective can help the transfer also to other sectors.

1.5. Aims

Finally, the main aim of this work was to perform a risk population assessment on rising temperatures and heat waves by Landsat LST timeseries in Aosta Valley, NW Italy by realizing a scalable application to all 18 countries that already have an HDX Meta dataset. The analysis was performed at a pixel level, grouping the final population exposure at a municipality level. It is worth noting that the map generated will be available at a pixel level.

Moreover, the quality of the population dataset was checked, and a risk map performed considering the population distribution and the LST gains modelized. In particular, LST maximum and mean trends were computed considering their significance, and possible correlations were tested considering the following parameters: (a) fractional vegetation cover (FVC), (b) quote, (c) slope, (d) aspect, and (e) potential incoming solar radiation (mean sunlight duration in the meteorological summer season) in order to assess which parameters include in the risk model.

The final outputs have permitted the mapping and assessment of the LST gain in the last 39 years (1984–2022) and relative population exposure to LST trends per age bands and gender groups, providing hopefully useful information to civil protection services and the health sector, permitting them to detect areas in which calls to health emergencies would be more likely during heatwaves and allowing urban planners to promote greening actions in a mitigation and adaptation perspective to climate change according to a One Health approach.

2. Materials and Methods

2.1. Aosta Valley Study Area

The study was carried out considering the Aosta Valley Autonomous Region in the northwest of Italy (please see Figure 1 below). To perform zonal statistics on the study territory, ESRI shapefile municipality boundaries were downloaded from the SCT Geoportale della Valle d'Aosta (https://geoportale.regione.vda.it/, last accessed on 22 March 2023) and adopted for the computation.
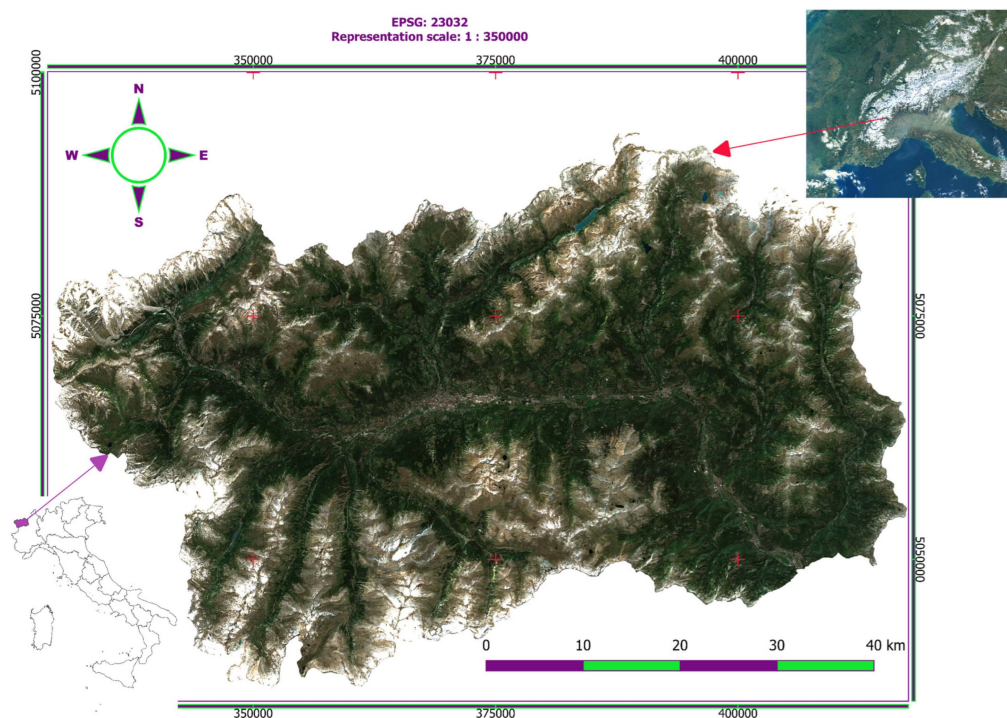
Figure 1. Study Area corresponding to the boundaries of the Aosta Valley francophone Autonomous Region (NW Italy).

2.2. Landsat Timeseries Datasets and LST Processing

LSTs have been computed from all Landsat missions that have been processed in Google Earth Engine (GEE). The United States Geological Survey (USGS) provides TOA brightness temperature images (hereinafter called Tb) as obtained from the thermal sensors of Landsat satellite missions. USGS Tb images collection 1 (from Landsat 4–5–7–8–9 missions, sensors TM, ETM+, TIRS) can be accessed through GEE. USGS also provides the corresponding at-the-surface reflectance-calibrated bands that can be, similarly, accessed

through GEE. Additionally, the quality-assessment band (BQA) is available too, making it possible to retrieve cloud coverage and shadowing information. All the bands are supplied with a ground sampling distance (GSD) of 30 m. Coarser thermal bands that natively have 100 m GSD have been oversampled by NASA using a bilinear approach at 30 m. The following GEE thermal collections were adopted to compute LST starting from brightness temperature:

(a)   USGS Landsat 4 Collection 2 Tier 1 TOA Reflectance (LANDSAT/LT04/C02/T1_TOA);
(b)   USGS Landsat 5 Collection 2 Tier 1 TOA Reflectance (LANDSAT/LT05/C02/T1_TOA);
(c)   USGS Landsat 7 Collection 2 Tier 1 TOA Reflectance (LANDSAT/LE07/C02/T1_TOA);
(d)   USGS Landsat 8 Collection 2 Tier 1 TOA Reflectance (LANDSAT/LC08/C02/T1_TOA);
(e)   USGS Landsat 9 Collection 2 Tier 1 TOA Reflectance (LANDSAT/LC09/C02/T1_TOA).

It is worth noting that, to compute LST from Landsat missions, TOA datasets bands B6 (from Landsat 4–5–7) and B10 (from Landsat 8–9) have been used.

Landsat data were processed in GEE [43] by adopting the approach proposed by [36]. Surface emissivity maps, needed for LST computation from Tb images, were obtained according to the Fractional Vegetation Cover (FVC) approach [64]. Therefore, to obtain FVC, NDVI was computed from surface-reflectance Landsat collections retrieved from all GEE collection products as follows:

(1)   USGS Landsat 4 Level 2, Collection 2, Tier 1 (LANDSAT/LT04/C02/T1_L2);
(2)   USGS Landsat 5 Level 2, Collection 2, Tier 1 (LANDSAT/LT05/C02/T1_L2);
(3)   USGS Landsat 7 Level 2, Collection 2, Tier 1 (LANDSAT/LE07/C02/T1_L2);
(4)   USGS Landsat 8 Level 2, Collection 2, Tier 1 (LANDSAT/LC08/C02/T1_L2);
(5)   USGS Landsat 9 Level 2, Collection 2, Tier 1 (LANDSAT/LC09/C02/T1_L2).

According to [36,64], FVC from NDVI and emissivity were computed as follows, respectively (collection from points 1 to 5). According to previous studies [65], NDVI was computed [66,67]:

$$\text{NDVI} = \frac{\text{NIR} - \text{RED}}{\text{NIR} + \text{RED}} \tag{1}$$

Fractional vegetation cover (FVC) was computed as follows:

$$\text{FVC} = \frac{\text{NDVI} - \text{NDVI}_S}{\text{NDVI}_V - \text{NDVI}_S} \tag{2}$$

where NDVIs and NDVI_v are the NDVI values corresponding to completely bare soil and vegetated pixels, respectively [68]. It is worth noting that NDVI_s and NDVI_v were set to 0.2 and 0.86, respectively.

$$\varepsilon = \text{FVC}\varepsilon v + (1 - \text{FVC}\varepsilon s) \tag{3}$$

where ε is the emissivity and $\text{FVC}\varepsilon v$ and $\text{FVC}\varepsilon s$ are the FVC values computed for a completely vegetated and a pure bare soil pixel, respectively.

Once emissivity maps were obtained for all the acquisitions, corresponding LST images were finally computed by the Statistical Mono-Window (SMW) algorithm from the Climate Monitoring Satellite Application Facility (CM-SAF). This technique uses an empirical relationship between T_b and LST [34], based on a linearization of the radiative transfer equation showing an explicit dependence from emissivity.

$$\text{LST} = A_i \left(\frac{T_b}{\epsilon} \right) + \frac{B_i}{\epsilon} + C_i \tag{4}$$

where T_b is the TOA brightness temperature, and ε is the surface emissivity. A_i, B_i, and C_i are coefficients modelling the Total Column Water Vapor (TCWV) effect on LST. These coefficients have been made available by the NCEP/NCAR re-analysis 1 project and can be accessed and used through GEE depending on the considered Landsat collection.

Landsat data were analyzed from 1984 to 2022 including, therefore, 39 years of Landsat data. All acquisitions have been considered with more than 900 images and bidirectional reflection disturbance compensated with a self-made function in GEE according to [69] regarding the NDVI. Clouds, shadows, and saturated pixels have been masked out by considering pixel quality and radiometric saturation layers for each scene. Since the merged Landsat collections were not equally distributed in time and are therefore not suitable to perform timeseries analysis due to temporal gaps. All data have been filtered with a Savitzky–Golay filter [70–72] and regularized with a monthly timestep on GEE by adopting the Open Earth Engine Library (OEEL). It is worth noting that the year 2012 was derived after creating yearly composites through linear interpolation as explained below.

Landsat images after November 2011 (last acquisition by Landsat 5) and before March 2013 (beginning of Landsat 8 mission) were retrieved by interpolation and regularization due to the lack of images during the period mentioned above. Landsat 7 data starting from 31 May 2003 onwards were not considered and therefore not included in the timeseries regularization phase due to the failure of the Scan Line Corrector (SLC) which has affected the usage of these images. The correction of SLC was not performed with the ENVI tool, despite there being an algorithm able to do it, because we processed them in GEE.

Then, yearly composite images were computed for each year in the time range 1984–2022 by using the ee.Reducer GEE function in order to obtain the mean and the maximum pixel values in each year.

It is worth noting that LST is normally and more accurately estimated by using nighttime-acquired images to avoid the effect of direct solar irradiation in case of study of UHI. Nevertheless, the present study has focused on LST maximum trends that normally occur during the day. Moreover, the risk and exposure to the population are higher during sunlight. For these reasons, this research has been focused on daytime LST.

From the LST stack, computed and regularized maximum and mean trends were modelled in [73] with a 1st-order polynomial and the significance of the related gain evaluated performing Pettitt's trend test in R Studio [62,74–76]. It is worth noting that only significant gain values were averaged at the class level (distribution of population in each municipality in the study area). Finally gain, offset, standard errors, and *p*-value maps were realized in order to join these data with the Meta Population dataset to assess population risk from rising temperatures.

2.3. HDX Meta Population Dataset

The HDX Meta Facebook Population dataset was obtained as follows. Under the assumption that buildings act as a proxy for where people live, Meta (previously known as Facebook) obtains population estimates on a country-wide level, with 1×1 arcsecond resolution (~30×30 m at the equator) and sensitivity to individual buildings, enabling accurate studies of population aggregation in rural areas. To enable global analysis, Meta has developed a building-detection model. The Meta pipeline consists of several steps: extraction of 64×64-pixel images (patches) around detected straight lines using a conventional edge detector, which reduces the amount of data for classification by a factor of approximately 4. A portion of those candidates are sampled across all countries and labeled as training and evaluation data for the CNNs. The computer vision models are trained on a single machine with four GPUs, whereas the classification runs on Meta Facebook's infrastructure on a CPU cluster. During this phase, three different types of CNN were used: a classification model based on the SegNet [50]; a feedback neural network (FeedbackNet) performing weakly-supervised segmentation of the satellite images enabling Facebook to obtain building footprints [50]; and a denoising network which is capable of improving the quality of the source data by removing high-frequency noise from the satellite imagery. The encoder–decoder-style SegNet is customized to perform the classification at the level of a patch. The encoder (a convolutional sub-network) is used to extract abstract information about the input, and the decoder (a deconvolutional sub-network) is trained to upsample the output of the encoder into a spatially meaningful probability map representing the

possibility of house existence in the input. The probabilities generated by the decoder are averaged over all spatial locations within the patch to derive the final classification, including GNSS tracking. This yields high accuracy and a reduced false positive rate on a global scale compared to other methods. To facilitate a generalized and scalable model, Meta employs weakly-supervised learning that takes the abundant and easy-to-acquire image-level categorical supervision (binary labeling) into training, and performs pixel-level prediction during deployment [50]. The methodology is motivated by the feedback mechanism in human cognition and recent advances of computational models in Feedback Neural Networks [50], which deactivates the non-relevant neurons within hidden layers of neural networks and achieves pixel-wise semantic segmentation. Both models are trained on 150,000 binary-labeled (building/no building) patches, randomly sampled from all countries and seasons, covering both rural areas and urban areas. The output layer was validated considering censuses at a country level, reaching a global overall accuracy of 98.3% [50]. Then these data have been yearly coupled with aggregated tracking from Meta phone applications (such as Instagram, Facebook, WhatsApp). These data can be accessed through Meta Data for Good (https://dataforgood.facebook.com/, last accessed on 19 April 2023). The format is raster (30 m GSD) or a dataframe, and the updating frequency is yearly or more under request. In each dataset the pixel value reports the population number according to a given characteristic.

To test the quality of the Meta population 2020 product in a rural and mountain area such as Aosta Valley Autonomous Region, in the northwest of Italy, this dataset was tested considering the 2020 census at municipality level in Aosta Valley. The HDX Meta Population dataset was considered as the predicted population while the regional census was the observed true population. For each municipality in Aosta Valley the Mean Absolute Error (MAE) was computed as follows:

$$\text{MAE} = \frac{\sum_{i=1}^{n}(p_i - o_i)}{n} \tag{5}$$

where p_i is the prediction (Meta Population), o_i is the observed true value (ISTAT Population), and n is the number of samples (in this case the number of Aosta Valley municipalities 74) see Table A1 in Appendix A.

The population dataset, properly processed, allowed the spatial distribution of the following variables to be obtained according to the international standard of the World Bank (see Table 1) and adopted into the present study.

Table 1. HDX Meta Population dataset properly processed structure.

Population Structure	Description
VDA general	Overall population within a pixel
VDA men	Male population within a pixel
VDA women	Women population within a pixel
VDA women of reproductive age 15–49	Women population in reproductive age between 15–49 years old
VDA elderly 60 plus	Population older than 60 years old
VDA children under 5	Children population younger than 5 years old
VDA youth 15–24	Young population aged between 15 and 24 years old

2.4. Other Geospatial Layers

Since LST trends can reasonably be affected by multiple factors, some of them were considered and a correlation was tested in order to decide if it was reasonable to develop a multivariate suitability model including all of them or not. A multiple-correlation analysis in R was performed considering population distribution according to the following parameters: (a) fractional vegetation cover (FVC), (b) altitude, (c) slope, (d) aspect,

(e) potential incoming solar radiation (mean sunlight duration in the meteorological summer season), (f) LST gain maximum, and (g) LST gain mean.

2.4.1. Fractional Vegetation Cover

Fractional vegetation cover was computed from Landsat data to calibrate the LST as previously reported. Moreover, to define the vegetation percentage in a single present layer used as possible input into the risk model, FVC was also estimated in ESA SNAP 8.0.0 open-source software, starting from Copernicus Sentinel-2A (S2A) images. In particular a mean composite multi-band image in the 2020 summer meteorological season (from 1 June to 31 August) was generated in GEE with the function .mean() after applying cloud and shadow masking, and the bidirectional reflectance distribution function (BRDF) with a self-made algorithm implemented in GEE. The composite output was exported from GEE, preserving the native resolution of each S2A band and then processed in ESA SNAP 8.0.0 by applying the Biophysical Processor S2_10 m function. FVC was considered in the model in order to assess if vegetation may have a mitigating effect on temperature trends [8].

2.4.2. Potential Incoming Solar Radiation and Terrain Analysis

As previously said, the population distribution was analyzed considering also the geomorphology and sun irradiance. In particular, altitude and duration of solar insolation have been considered. In order to retrieve these two parameters, the Aosta Valley Digital Terrain Model (DTM) and Digital Surface Model (DSM) retrieved from aerial Lidar flight during 2005/2008 were adopted. These datasets, with a native spatial resolution of 2 m, were oversampled at 30 m with a bilinear interpolation, as described in [73]. The DTM was used to map the altitude while the DSM was used to map the duration of insolation at pixel level as a mean of the entire 2020 meteorological summer season. In Table 2 the settings parameters adopted are reported:

Table 2. Modelling solar duration.

Solar Constant (Wm^{-2})	1367
Time Period	Range of days
Start day	1 June 2020
End day	31 August 2020
Resolution (day)	1
Time Span (h)	24
Resolution (h)	0.5
Atmospheric Effects	Lumped Atmospheric Trasmittance

To detect surface height, the regional deep learning dataset realized in 2020 was adopted. In fact, this dataset contains the buildings patches, with their heights, on the Aosta Valley territory. Slope and aspect were computed from the Aosta Valley Digital Terrain Model (DTM) freely available in the SCT Geoportale della Regione Autonoma Valle d'Aosta (https://geoportale.regione.vda.it/, last accessed on 30 January 2023) in SAGA GIS v.8.5.0.

2.5. Geostatistical Analysis

Before performing geostatistics and modeling LST trends, a normal distribution test was executed to understand the type of data. In particular, a Kolmogorov–Smirnov test concerning LST profile time-series was performed in R. Then, a self-made script in R Studio was adopted to map gain, offset, and *p*-value (Pettitt's test). Pettitt's test was carried out because, as indicated in the workflow, only the significant pixels were modeled. Therefore, thanks to it, break points were identified in the time series. In LST max and mean gain layers, pixels not significant were masked out considering only significant Pettitt's *p*-value < 0.05 (hereinafter called CM) after clipping the data onto the Population dataset. Subsequently, the ISODATA unsupervised classification–clustering algorithm was performed on CM and

the separability of each class obtained was checked by computing the Jeffries–Matusita (J-M) distances as follows:

$$JM_{ub} = \sqrt{2(1 - e^{-\alpha})} \tag{6}$$

$$\alpha = \frac{1}{8}(\mu_u - \mu_b)^T \left(\frac{C_u + C_b}{2}\right)^{-1}(\mu_u - \mu_b) + \frac{1}{2}\ln\left[\frac{\frac{1}{2}|C_u + C_b|}{\sqrt{|C_u| \times |C_b|}}\right] \tag{7}$$

where:

u and b: the classes to separate,
C_u: the covariance matrix of u,
μ_u: the mean vector of u,
T: transposition function.

The same procedure was applied to the FVC, solar duration, quote, aspect, and slope. Each cluster (hereinafter called CLU) generated was considered in the model only if it had a strong and statistically significant correlation to the other to assess population exposure by performing zonal statistics in SAGA GIS v.8.5 [73]. All the input data have been normalized. The maximum number of iterations has been set to 20 while the initial number of clusters and samples in the cluster is 5 and the maximum number of clusters is 16. Finally, in each CLU, zonal statistics considering Aosta Valley municipalities were performed. In particular, to assess rising temperature exposure, the following procedure was deployed:

$$Rexp = CLU_{LST_{gain}}(x, y) \cap Meta_{pop}(x, y) \tag{8}$$

where:

R_{exp} is the risk exposure;
$CLU_{LSTgain}$ is the Cluster performed on LST maximum and mean significant layer respectively;
$Meta_{pop}$ is the Meta population processed dataset.

Since in each municipality different clusters of the same type were present after performing Equation (8) to define the risk exposure in each municipality, considering each type of cluster, a pivot spatial table was realized by using the Group Stat tool available in QGIS.

Moreover, a suitability risk map modeler was realized and performed starting from native input datasets to map rising temperature risk exposure. An analytic hierarchical process (AHP) was followed, and it was decided that only correlated and significant variables would be tested after performing a multivariate geostatistical analysis (see in Section 3). The risk was mapped as follows:

$$R_{exp} = \{[(Z_\alpha(x, y) \times \omega_\alpha) + (Z_\beta(x, y) \times \omega_\beta) + (Z_\gamma(x, y) \times \omega_\gamma)] \times 100\} \tag{9}$$

$$\omega = \frac{M}{(n + M - 1)} \tag{10}$$

where R_{exp} = risk exposure.

$$TfMSSmallZ = \frac{\sigma \times \vartheta}{[X - (\tau \times \mu) + (\sigma \times \vartheta)]}$$

where:

σ = standard deviation;
μ = mean;
ϑ = a σ multiplier;
τ = a μ multiplier;
ω = input value;

ω = the weight defined in each input (in this case 0.333);

M = the maximum of the AHP scale;

n = the number of criteria (in this case 10);

α, β, γ = the three input datasets respectively (LST Gain mean, LST Gain max, and DSM).

3. Result

The first phase was to check the consistency of the Meta Population dataset. Therefore, the MAE was computed as reported in Equation (5). The predictor was assumed to be the Meta Population dataset and the true value data to be the ISTAT Population in each Aosta Valley municipality. In Appendix A (in Table A1) we report the MAE results obtained. The dataset seems to have a consistency by observing the results obtained. Moreover, the gender and age distribution were tested but not reported showing a strong consistency. After checking the quality of the population dataset and modeling the LST maximum and mean trend and defining their significance, correlations were tested considering the following parameters: (a) fractional vegetation cover (FVC), (b) quote, (c) slope, (d) aspect, and (e) potential incoming solar radiation (mean sunlight duration in the meteorological summer season). In Figure 2 we report the results obtained. LST gain mean and maximum are positively and strongly correlated with each other, as computed by their linear R Pearson coefficient, as well as slope (but with a negative correlation). Moreover, they are statistically significant, with *p*-value < 0.05. The other variables have a lower Pearson correlation coefficient and are not statistically significant. Therefore, we decided to model population distribution in each variable but computed the risk exposure model in two ways: the first as reported in Equation (8) considering only the LST gain and clustering them, and then computing and mapping each Aosta Valley municipality, taking into account the population involved according to their structural parameters (please see Table 1); the second way was by mapping, with a suitability model, the population risk exposure as reported in Equation (9).

In the tables below (see Table 3), the ISODATA clustering performed per LST Gain Max has been reported, which represents the major risk exposure in a given area with the optimal number of clusters with their mean range, standard deviation, and distance. It is worth noting that, onto these clusters, Equation (8) was computed, a map generated, and zonal statistics performed by realizing a pivot spatial analysis onto population datasets at municipality level. In this work only LST Gain Max tables have been reported due to the fact that they represent the extreme conditions.

Table 3. LST Clusters.

Cluster ID	Mean Gain LST Max (°C)	StDev Gain LST Max	Exposure–Risk Class Assessment	Mean Distance
1—I	0.21	0.00	7	0.05
2—II	0.01	0.04	1	0.28
3—III	0.19	0.01	6	0.06
4—IV	0.27	0.02	9	0.10
5—V	0.23	0.01	8	0.08
6—VI	0.17	0.01	5	0.08
7—VII	0.10	0.02	3	0.07
8—VIII	0.31	0.04	10	0.16
9—IX	0.07	0.00	2	0.13
10—X	0.13	0.00	4	0.09
11—XI	0.38	0.00	11	0.29

In the figure below, the maps obtained from Equation (8) and from which Table A2 in Appendix B was obtained have been reported. The exposure-risk class assessment reported in the map was defined considering the gain values, from major to minor, where higher gain values have higher class numbers. Consider Figures 3 and 4.
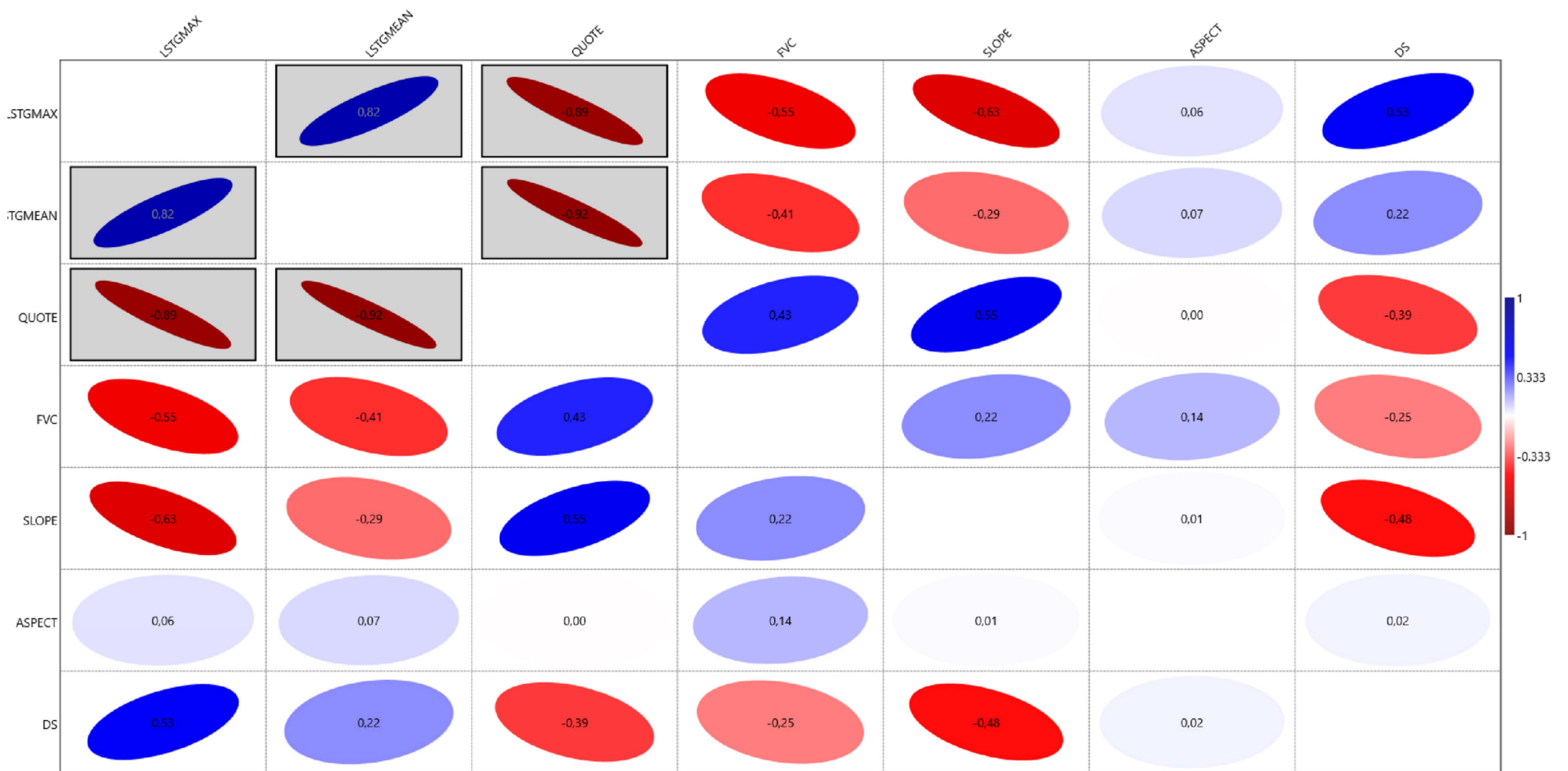
Figure 2. Multiple correlation testing involving LST Gain Maximum, LST Gain Mean, Quote, FVC (Fractional Vegetation Cover), Slope, Aspect, Sun Duration (DS). Positive correlation is in blue, negative in red. Rectangles represent statistically significant *p*-value < 0.05.
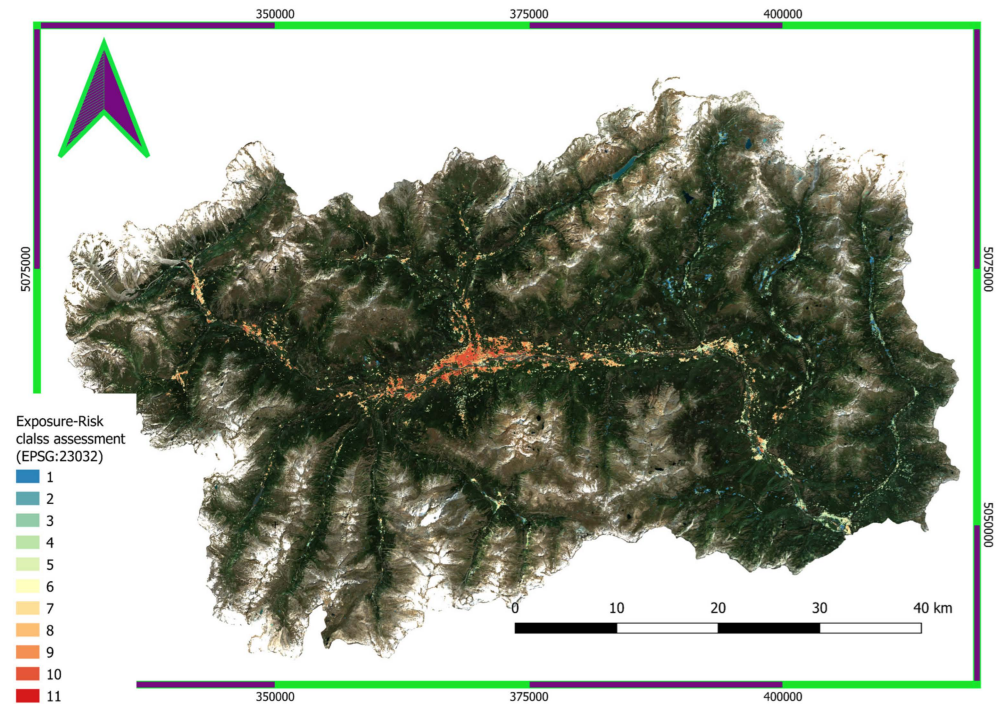
Figure 3. Exposure-Risk class assessment map (scale 1:3,300,000). EPSG: 23032.
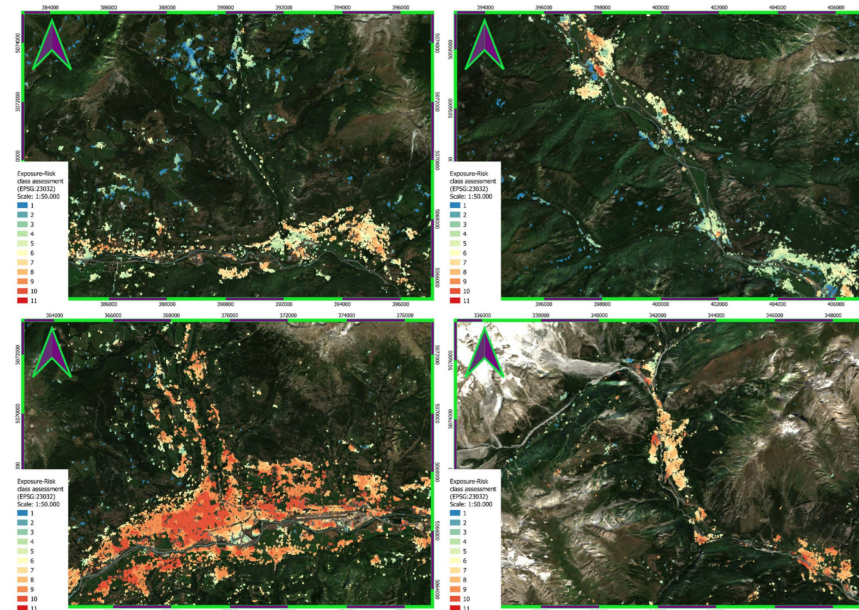
Figure 4. Exposure-Risk class assessment map (with some zooms in in the bottom valley from East to West with a scale of 1:50,000). EPSG: 23032.

Then, as reported previously, a risk map was developed by adopting Equation (9). In this last case the map produced from the suitability risk modeler has considered not only LST gain maximum such as those in Figures 3 and 4 but also LST gain mean and quote, due to the fact that they have been tested as previously described. It is worth noting that the model developed suggests a risk exposure to rising LST, taking into consideration the variables previously described in risk-exposure ranges between 0 and 100%, where 100% is the maximum risk exposure considered according to the input parameters considered in the model. In these areas, attention must be paid to the high risk represented by the LST trends and their locations. In these areas, the emissivity of the materials, and consequently their

albedo, is very different from those with materials that are able to mitigate heatwaves and LST trends. The results obtained have permitted the population involved to be mapped, thanks to the zonal statistics performed adopting the HDX Meta population dataset.

From these last maps obtained from the risk modeler developed, it is possible to see how more than 60% of the Aosta Valley population, who mostly live in the bottom of the valley, are exposed to a risk of rising temperature and heatwaves with a probability greater than 55%. These effects have and will have important socio-economic impacts, not only on the health sector but also on pets and domestic animals (particularly if we consider that one of the main items of the GDP of Aosta Valley comes from animal husbandry and how, therefore, certain breeding farms and related production and animal welfare are more at risk than others, although the practice of summer pasture can mitigate this through a mechanism of escape from mapped and modeled thermal trends) (please see Figures 5 and 6).
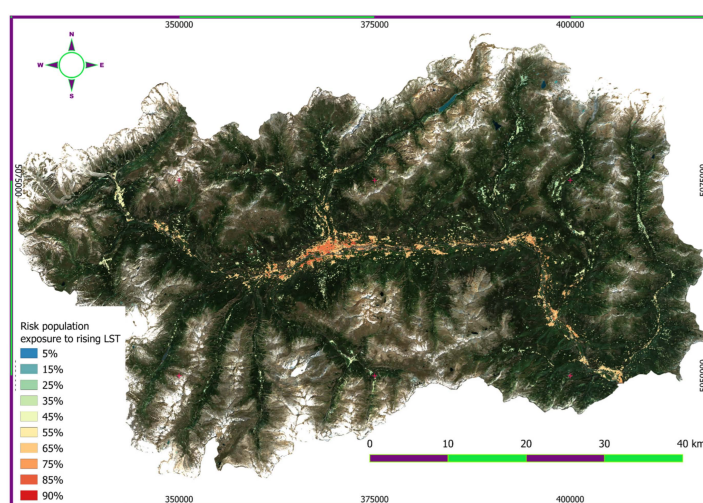
Figure 5. Risk population exposure to rising LST mapped according to Equation (9). EPSG: 23032.
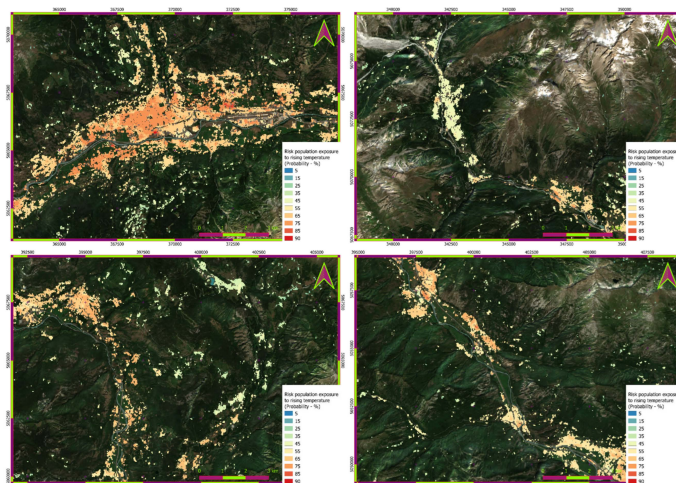
Figure 6. Risk population exposure to rising LST mapped according to Equation (9) (with zooms in given areas with a scale of 1:50,000), EPSG: 23032.

4. Discussion

The results obtained constitute a first example on the Aosta Valley territory of climate risk assessment through the use of a unique high-resolution dataset (being currently the most detailed raster data for scientific applications). Moreover, the Meta dataset has never been used until today, based on the information available in the scientific literature, in this

way. A combined use with Earth observation data or weather station data can certainly be an important tool of added value in the creation of new information layers and GIS and risk analysis. The maps obtained can thus represent added value in the context of upgrading hospitals and clinical outpatient clinics, or even from an urban planning perspective with regard to urban-greening policies and actions. We hope this instrument will have added value for civil defense. Certainly, a future development that focuses on individual buildings taking into consideration increasingly timely data of population and physical characteristics of surfaces is desirable so as to provide more and more detailed, but most importantly up-to-date, data.

In this study, it is worth noting that the HDX Meta population dataset from empirical ground data collected by some municipalities in Aosta Valley seemed to be more accurate in terms of people that are present in a given area than the ISTAT residents. In fact, many people are resident in a given municipality but live in a different municipality in which they are domiciled. Therefore, a population dataset based on a tracking system seems to better fit the real population distribution which still remains a great challenge considering also privacy policies.

Given the quality of the data, an increasingly up-to-date and detailed population dataset at both spatial and temporal resolution levels is desirable for studies of this kind. Moreover, cross-referencing such data with geo-referenced animal population data would certainly allow the development of models of the risk to domestic animals and their productivity in the case of non-pet animals, while also allowing the development of new lines on animal welfare with a view to adapting to climate change while avoiding stresses such triggering possible disease from a weakened situation.

Nowadays, in fact, there is no high-detail geospatial dataset of both domestic and affectionate animal populations (such as cats and dogs) at a global level. A datum of this kind would allow not only a modeling of climate risk but also, and above all, health risk in the case of zoonosis and eco-epidemiology towards a real and concrete application of One Health. It is worth noting that the implementation would not be complex, considering that in many countries there is an obligation to chip pets and in the case of livestock there is a specific registry managed by veterinary services.

Surely a global effort in this direction together with a high temporal resolution and good detail mapping of the population with information aggregated in respect of privacy would allow a significant technological transfer to the health sector through cross studies for health and risk analysis related to the effects of climate change. In this case, an application on a local scale was attempted, also testing the quality of the population dataset. Surely, future missions such as those from the Albedo enterprise which will provide thermal data with GSD 2 m (if they will be made free for applied scientific research) will allow extremely detailed studies if they are accompanied by other very-high-resolution information datasets. With the data currently in possession, however, precious information can be obtained from a planning and management point of view. It still seems difficult and complex to suggest punctual actions at the sub-district level. In fact, it must be said that the Landsat data have a thermal resolution at 30 m, equal to 900 square meters but resampled by NASA and that the thermal sensors have an average resolution of 100 m, equal to an area of one hectare.

Currently the only scientific mission with a higher-resolution thermal sensor, ECOSTRESS on board the International Space Station, does not allow long-term studies and was mainly designed as a tool for monitoring vegetation. Unfortunately, other scientific missions that make satellite data available free of charge, such as the European space program's Copernicus, have thermal data that are not suitable for conducting detailed studies. In fact, Sentinel-3 has a GSD of 1 Km. The development of high thermal resolution sensors with free access data would be desirable. Only the Albedo company is currently investing in high-resolution commercial satellite data as previously said, but it is not yet known whether its distribution policies will be free for research. However, in a mitigation and adaptation perspective to climate change, their implementation is not only desirable on a global level but also strategic in defining concrete One Health actions [77–79]. It is worth noting that

mapping the exposure of population involved according to different levels of temperature (LST) gain permits greening actions and policies to be addressed, favors the identification of new medical or health centers, predicts in advance the areas that will be more subject to emergency calls, redevelops areas or zones most at risk with a view to mitigation and above all adaptation, makes forecasts on access to hospitals in case of heat waves and the impact of costs on the health sector having mapped data, and evaluates the effectiveness of requalification policies and actions and its effects on heat flows and on the risk associated with the exposed population. Nevertheless, at the present time, analyses of exposures to thermal trends are linked to EO data with GSD at 30 m (natively 100 m resampled at 30 m in case of Landsat). They currently represent the highest resolution available for scientific purposes. The hope is that the missions of the private company Albedo, which will provide satellite thermal data at 2 m GSD, will be free for scientific purposes and will allow a significant technological and application leap. An increasingly detailed population dataset is also desirable, although the aggregate Meta dataset is currently the most detailed from a spatial point of view. To date, in fact, although the present application is notable, it still limits the analyses at a cluster level by areas, making analyses at a building level more complex, which would certainly be desirable for the future. In fact, mapping the risk at the level of a single residential structure and its surroundings would allow increasingly precise actions with a view to adaptation and capillary and punctual analysis of the risk.

Concerning the present study, it is interesting to see how the bottom of the valley is more affected by rising temperature and how FVCs do not play a statistically significant role (probably this is due to the fact that Landsat pixel GSD does not permit one to appreciate in urban areas the effect offered by sparse vegetation (that normally, considering the study area, is less than half a pixel). It is interesting to know how most of the highly risk areas are located in industrial areas and in modern buildings rather than in historical buildings. At the same time, it is interesting to underline from a civil protection perspective how more than 60% of the Aosta Valley population (mostly concentrated in the valley floor for work reasons) is in high exposure and risk classes with both approaches adopted. Although in the summer some prefer to find refuge in the side valleys, the fact that a large part of the mostly elderly population is exposed to a greater risk should lead to rethinking urban planning and the creation of services or assistance hubs in areas with greater exposure. We hope to see a major application of EO Data in a One Health perspective [80].

Regardless of the considerations on the planning developments of climate adaptation and mitigation, we hope that this study will be useful and can also be scaled to other realities and become more and more detailed.

5. Conclusions

The rising temperatures due to the effects of climate change require the rapid development of adaptation and mitigation plans and concrete actions. In this study, an attempt was made for the first time by coupling the HDX Meta population dataset and free satellite data from the USGS NASA Landsat 4–9 missions. In particular LST trends were used to map the exposure and risk deriving from the increase in temperatures in Aosta Valley, the smallest region of Italy but one of the hardest hit by the effects of climate change. The developed approaches can be scaled to other realities and at national and international level by enhancing not only the Meta data but also by promoting a technological and knowledge transfer to the health and environmental sector through concrete tools useful for tackling climate change. In the case of the Aosta Valley, the punctual mapping of the risk and trend of exposure to temperatures has made it possible, thanks to the Meta dataset, to define risk and exposure classes according to the distribution and structure of the population at the municipal level which we hope will be useful to the sector of civil protection and medical-health including veterinary. If we think of domestic and bred animals, their spatial distribution has not been considered. Therefore, further studies on them as well as more and more punctual monitoring of the population with increasingly updated data are

certainly desirable in the climate change framework adaptation and mitigation planning, adaptation and policies.

Finally, results have shown a steeper increase in LST maximum trend, especially in the bottom valley municipalities, and especially in new built-up areas around factories where more of 60% of the Aosta Valley population (especially elderly and younger people) live and where a high exposure risk has been detected and mapped with both approaches performed. We strongly hope that maps produced may help the local planners and the civil protection services to face global warming in a One Health perspective. Last but not least, we hope this type of application may become ordinary and useful to other regions, countries, studies, and more in general realities enhancing the exploitation of a combined use of free satellite data and population data social tracking for the purposes of rational territorial planning and management according to a real One Health approach.

Appendix A

Below, the MAE computed considering the HDX Meta Population dataset and the ISTAT population data is reported:

Table A1. Population validation.

ID Italian Municipality	Municipalities in Aosta Valley Region	HDX Meta Population 2020 (p_i)	ISTAT Effective Resident on 31 December 2020 (o_i)	MAE
A205	Allein	244	210	34
A305	Antey-Saint-Andre	645	565	80
A326	Aosta	33,204	33,916	−712
A424	Arnad	1278	1245	33
A452	Arvier	917	870	47
A521	Avise	378	306	72
A094	Ayas	1406	1393	13
A108	Aymavilles	2266	2104	162
A643	Bard	110	122	−12
A877	Bionaz	224	225	−1
B192	Brissogne	1034	948	86
B230	Brusson	792	883	−91
C593	Challand-Saint-Anselme	804	758	46
C594	Challand-Saint-Victor	618	548	70
C595	Chambave	908	919	−11
B491	Chamois	92	98	−6

Table A1. *Cont.*

ID Italian Municipality	Municipalities in Aosta Valley Region	HDX Meta Population 2020 (p_i)	ISTAT Effective Resident on 31 December 2020 (o_i)	MAE
C596	Champdepraz	742	714	28
B540	Champorcher	365	394	−29
C598	Charvensod	2688	2338	350
C294	Chatillon	5023	4524	499
C821	Cogne	1403	1377	26
D012	Courmayeur	2759	2761	−2
D338	Donnas	2551	2448	103
D356	Doues	580	512	68
D402	Emarese	247	223	24
D444	Etroubles	539	481	58
D537	Fenis	1860	1769	91
D666	Fontainemore	472	431	41
D839	Gaby	496	460	36
E029	Gignod	2094	1715	379
E165	Gressan	3819	3393	426
E167	Gressoney-La-Trinite	315	318	−3
E168	Gressoney-Saint-Jean	815	812	3
E273	Hone	1170	1189	−19
E306	Introd	696	661	35
E369	Issime	430	407	23
E371	Issogne	1405	1349	56
E391	Jovencan	895	723	172
A308	La Magdeleine	129	109	20
E458	La Salle	2200	2001	199
E470	La Thuile	810	812	−2
E587	Lillianes	444	445	−1
F367	Montjovet	1864	1802	62
F726	Morgex	2166	2096	70
F987	Nus	3228	2950	278
G045	Ollomont	150	165	−15
G012	Oyace	223	217	6
G459	Perloz	413	457	−44
G794	Pollein	1617	1536	81
G854	Pontboset	185	173	12
G545	Pontey	907	801	106
G860	Pont-Saint-Martin	4014	3592	422
H042	Pre-Saint-Didier	1031	1031	
H110	Quart	4601	4045	556
H262	Rhemes-Notre-Dame	111	85	26
H263	Rhemes-Saint-Georges	192	174	18
H497	Roisan	1217	1038	179
H669	Saint-Christophe	3598	3446	152
H670	Saint-Denis	399	382	17
H671	Saint-Marcel	1385	1365	20
H672	Saint-Nicolas	311	320	−9
H673	Saint-Oyen	240	199	41
H674	Saint-Pierre	3512	3195	317
H675	Saint-Rhemy	328	329	−1
H676	Saint-Vincent	4509	4432	77
I442	Sarre	5497	4817	680
L217	Torgnon	525	567	−42
L582	Valgrisenche	198	196	2
L643	Valpelline	691	618	73
L647	Valsavarenche	187	175	12
L654	Valtournenche	2037	2255	−218
L783	Verrayes	1389	1264	125
C282	Verres	2712	2577	135
L981	Villeneuve	1380	1259	121
	Aosta Valley Region	130,683	125,034	76

Appendix B

Below we report the number of people and their relative structure exposed to each class of rising temperature (LST) in each Aosta Valley municipality:

Table A2. Risk assessment defined by adopting the first method (see Equation (8)).

ID Italian VDA Municipality	Cluster ID—Mean Gain LST Max—n° Population Exposed VDA General										
	I	II	III	IV	V	VI	VII	VIII	IX	X	XI
A205	34		65		17	86	6		3	33	
A305	4	16	75	1		231	65		38	215	
A326	166	4	138	2805	546	66	7	12,346	13	45	17,069
A424	326	3	436	17	94	155	69	3	57	117	
A452	12		9	534	171	4		186		1	
A521	64		32	95	143	10	21	2	1	10	
A094	32	58	103	2	4	160	302	1	396	350	
A108	32		26	529	122	11		1203		3	340
A643	14		23			29	17			29	
A877	17	1	55	23	31	47	8	5	17	20	
B192	44		54	427	178	39	1	281		2	8
B230	7	6	144		1	304	58		61	211	
C593	184		219	11	127	176	13		4	71	
C594	36		13	295	143	9		119		3	
C595	151	1	232	128	195	115	2	65		18	
B491		3				1	27		29	32	
C596	214	1	217	6	114	164	4		3	18	
B540		58				2	76		120	109	
C598	68		70	609	170	32		1476		1	263
C294	785	6	1356	611	1352	843	4	32	4	31	
C821	235	11	275	41	347	249	65	5	31	144	
D012	224		161	1036	944	76		179		3	135
D338	69		788	1	1	1289	32		3	367	
D356	39		41	233	104	28	2	123		8	1
D402	33	2	62			49	3		5	93	
D444	114	1	97	163	141	18			1	3	
D537	103		28	986	604	15		122		1	
D666	38	9	105		3	193	24		18	82	
D839		4	84			238	40		8	122	
E029	162	3	116	492	364	127	22	661	24	96	29
E165	53		64	230	165	70	1	1723		25	1488
E167	4	20	10		1	21	86		129	43	1
E168	2	18	14			141	202		184	253	
E273	48	9	291	24	28	492	58	16	22	183	
E306	64	1	51	233	304	21	2	11	2	8	
E369	15	22	36		3	150	32		55	116	
E371	344	25	326	10	411	154	41		31	63	
E391				40				502			352
A308		6				11	23		69	20	
E458	164		102	711	393	28	2	790	1	4	5
E470	34		27	364	240	3		142			
E587	8	4	162			210	8		10	41	
F367	302		250	471	737	61	1	36	1	5	
F726	32		8	769	150	4		976		3	225
F987	221	1	159	1368	612	104	15	558	23	46	121
G045	22		2	67	43	1		14		1	
G012	31		15	71	83	19				3	
G459		4	27			203	31		8	141	
G794	15		3	575	102	3	1	871		2	44
G854		3				37	67		7	72	
G545	126		89	143	532	8				9	

Table A2. *Cont.*

ID Italian VDA Municipality	Cluster ID—Mean Gain LST Max—n° Population Exposed VDA General										
	I	**II**	**III**	**IV**	**V**	**VI**	**VII**	**VIII**	**IX**	**X**	**XI**
G860	1017	3	1525	165	507	691	27		7	72	
H042	86		38	318	365	8	3	182	2	6	25
H110	220	2	208	1912	692	102	17	1209	6	51	182
H262	18		18	1	7	32	2			32	
H263	37		27	20	65	28			3	11	
H497	11		1	670	92	1		440			
H669	17		45	737	64	2		2340			391
H670	45	11	46	35	59	63	35	7	28	71	
H671	69	1	79	651	226	28	4	308	3	10	6
H672	38		55	97	93	10	5	4		8	
H673	14		59		3	82	24		13	46	
H674	16	12	16	830	77	34	17	1773	17	21	700
H675	29		37	24	40	140	2	12		41	3
H676	801	3	403	884	2068	117	34	93	22	83	
I442	178	1	128	1655	358	139	4	2338	16	42	640
L217		56	6				28	141		134	159
L582	35		15	49	87	4		4		2	2
L643	94		87	202	185	22	1	93		6	2
L647	51	1	21	19	46	29	1	2	1	16	
L654		81	73			426	381		358	717	
L783	191	8	242	75	234	310	95	7	43	184	
C282	714	1	591	394	449	265	3	167	2	91	35
L981	70		40	475	198	9	1	553		1	34
VDA overall	8443	480	10,420	23,334	15,635	9077	2235	31,980	2033	4946	22,101
VDA overall %	6.5	0.4	8.0	17.9	12.0	6.9	1.7	24.5	1.6	3.8	16.9

ID Italian VDA Municipality	Cluster ID—Mean Gain LST Max—n° Population Exposed VDA Men										
	I	**II**	**III**	**IV**	**V**	**VI**	**VII**	**VIII**	**IX**	**X**	**XI**
A205	17		33		6	46	3		1	16	
A305	2	9	34			114	32		19	105	
A326	86	2	72	1381	274	35	4	5852	7	23	7704
A424	155	1	203	8	43	73	34	1	29	56	
A452	6		4	273	84	2		96		1	
A521	31		16	45	69	6	10	1	1	5	
A094	17	31	54	1	2	80	154		194	174	
A108	16		12	262	61	5		597		1	168
A643	6		11			13	8			13	
A877	9		29	12	16	27	4	2	7	12	
B192	26		28	218	92	21		144		1	4
B230	4	4	70			142	29		30	98	
C593	90		107	6	63	90	7		2	38	
C594	18		7	147	73	5		61		2	
C595	75	1	113	67	99	56	1	34		10	
B491		2				1	13		14	15	
C596	100	1	103	3	57	79	2		2	9	
B540		27				1	37		59	56	
C598	35		37	303	86	17		731			131
C294	375	3	658	303	656	413	2	15	2	15	
C821	115	5	135	20	177	123	33	2	15	70	
D012	113		84	510	468	40		90		1	71
D338	33		371		1	615	16		2	179	
D356	19		20	114	51	14	1	58		4	1
D402	15	1	33			26	2		2	53	
D444	58	1	49	83	71	9				2	
D537	51		14	500	297	7		63		1	
D666	20	5	53		2	97	13		10	42	
D839		2	42			115	21		4	58	

Table A2. *Cont.*

ID Italian VDA Municipality	Cluster ID—Mean Gain LST Max—n° Population Exposed VDA General										
	I	**II**	**III**	**IV**	**V**	**VI**	**VII**	**VIII**	**IX**	**X**	**XI**
E029	78	1	60	233	175	68	12	326	12	50	15
E165	29		34	116	89	36		859		12	735
E167	2	8	5			10	40		56	21	1
E168	1	8	6			68	100		90	125	
E273	24	4	137	11	14	234	27	8	11	87	
E306	32		26	119	147	10	1	6	1	4	
E369	8	12	18		1	72	16		28	57	
E371	167	12	157	5	203	74	20		15	29	
E391				21				255			181
A308		3				6	13		36	12	
E458	82		50	352	199	14	1	386		2	2
E470	18		14	179	119	2		70			
E587	4	2	74			99	5		5	21	
F367	156		131	239	381	31	1	18		3	
F726	17		4	378	70	2		474		1	105
F987	111		82	662	302	52	8	270	13	24	60
G045	10		1	36	21			8			
G012	16		9	37	46	13				2	
G459		2	12			96	18		5	70	
G794	8		2	289	52	2	1	434		1	22
G854		2				17	35		4	34	
G545	62		43	69	266	4				5	
G860	497	2	740	78	244	335	14		4	39	
H042	43		18	167	187	4	2	94	1	3	12
H110	113	1	108	958	347	53	9	606	4	27	98
H262	10		9	1	4	20	1			21	
H263	18		13	10	32	14			2	6	
H497	5			337	46			218			
H669	8		22	361	31	1		1149			193
H670	22	6	23	18	29	33	18	4	16	38	
H671	34		39	319	112	14	2	151	2	6	3
H672	18		31	49	44	5	3	2		4	
H673	7		28		1	39	11		6	22	
H674	8	6	8	412	38	18	9	889	9	10	350
H675	16		20	12	20	77	1	6		23	2
H676	396	2	203	429	995	61	18	46	10	42	
I442	89	1	64	801	180	70	2	1148	13	20	316
L217		27	3			15	75		70	82	
L582	18		8	24	46	3		2		1	1
L643	50		46	107	98	11		50		3	1
L647	23		10	9	20	15	1	1		9	
L654		38	37			217	201		184	380	
L783	98	4	125	39	120	158	47	4	21	90	
C282	346	1	286	195	217	126	2	82	1	43	17
L981	36		20	246	100	5	1	281		1	17
VDA overall	4172	237	5118	11,574	7744	4476	1141	15,594	1019	2490	10,210
VDA overall %	6.5	0.4	8.0	18.1	12.1	7.0	1.8	24.5	1.6	3.9	16.0

ID Italian VDA Municipality	Cluster ID—Mean Gain LST Max—n° Population Exposed VDA Women										
	I	II	III	IV	V	VI	VII	VIII	IX	X	XI
A205	17		32		10	41	3		2	17	
A305	2	7	40	1		117	33		19	110	
A326	80	2	66	1423	273	31	3	6493	6	21	9365
A424	172	2	233	9	50	82	35	1	29	61	
A452	6		5	261	88	2		90		1	
A521	33		16	49	73	4	11	1		5	
A094	15	27	49	1	2	79	148		201	176	

Table A2. *Cont.*

ID Italian VDA Municipality	Cluster ID—Mean Gain LST Max—n° Population Exposed VDA General										
	I	II	III	IV	V	VI	VII	VIII	IX	X	XI
A108	16		14	267	61	6		606		2	173
A643	7		12			15	9			15	
A877	8		26	11	15	20	4	3	10	8	
B192	18		26	209	85	17		137		1	4
B230	4	3	74			161	29		30	112	
C593	94		112	5	63	86	6		2	32	
C594	18		6	148	70	4		58		1	
C595	75	1	119	61	96	59	1	31		9	
B491		1				1	14		15	17	
C596	114	1	114	3	57	85	2		1	9	
B540		31				1	39		61	53	
C598	32		33	306	83	15		746			132
C294	410	3	698	308	695	431	2	17	2	15	
C821	121	5	140	20	170	126	32	2	16	74	
D012	111		77	526	477	36		90		1	64
D338	36		417		1	674	15		1	187	
D356	20		21	119	53	14	1	65		4	
D402	19	1	29			23	1		2	39	
D444	56	1	48	81	70	9				2	
D537	53		14	486	307	8		59		1	
D666	18	4	53		2	95	11		8	40	
D839		2	43			124	18		3	64	
E029	83	2	56	259	189	59	10	335	12	46	14
E165	24		29	114	77	34	1	864		12	753
E167	2	12	5			11	46		73	22	1
E168	1	11	8			73	102		94	128	
E273	25	5	154	12	14	257	30	8	11	96	
E306	32		26	114	157	11	1	5	1	4	
E369	8	10	18		1	78	16		26	59	
E371	177	13	169	5	208	80	21		16	34	
E391				20				247			171
A308		3				4	10		33	9	
E458	82		51	359	194	14	1	405		2	3
E470	17		13	184	121	1		72			
E587	5	2	87			111	3		5	20	
F367	146		120	232	355	29	1	17		3	
F726	15		4	391	80	2		502		2	120
F987	109		77	706	311	51	7	289	9	22	60
G045	12		1	32	22			5			
G012	14		7	34	37	6				1	
G459		1	14			107	13		3	71	
G794	7		1	287	50	2	1	437		1	22
G854		1				20	32		2	38	
G545	64		46	75	266	4				4	
G860	521	1	785	87	263	356	13		3	32	
H042	43		20	151	178	4	2	87	1	3	13
H110	107	1	100	954	345	49	8	602	2	24	84
H262	8		9		3	13	1			11	
H263	19		14	10	33	14			1	5	
H497	6		1	333	46	1		222			
H669	9		24	376	33	1		1192			198
H670	22	5	23	17	30	30	17	4	12	33	
H671	35		40	332	113	14	2	156	1	4	3
H672	20		24	49	50	5	2	2		4	
H673	7		31		1	43	13		7	24	
H674	9	5	9	418	38	16	8	883	8	11	350
H675	13		17	12	20	63	1	6		19	2

Table A2. *Cont.*

ID Italian VDA Municipality	Cluster ID—Mean Gain LST Max—n° Population Exposed VDA General										
	I	II	III	IV	V	VI	VII	VIII	IX	X	XI
H676	405	2	200	456	1073	57	16	46	12	40	
I442	89		63	854	179	68	1	1190	3	22	323
L217		29	3			14	66		65	77	
L582	17		7	24	41	1		1		1	
L643	44		41	95	86	11		43		3	1
L647	28		11	10	26	14		1		7	
L654		44	36			209	180		174	337	
L783	93	4	116	37	114	152	48	3	22	94	
C282	368	1	305	199	232	139	1	85	1	48	18
L981	34		20	230	98	3		271			17
VDA overall	4274	244	5304	11,763	7890	4597	1094	16,384	1008	2451	11,892
VDA overall %	6.4	0.4	7.9	17.6	11.8	6.9	1.6	24.5	1.5	3.7	17.8

ID Italian VDA Municipality	Cluster ID—Mean Gain LST Max—n° Population Exposed VDA Women of Reproductive Age 15–49										
	I	II	III	IV	V	VI	VII	VIII	IX	X	XI
A205	8		13		7	12	1			4	
A305	1	3	18			51	14		9	51	
A326	36	1	30	610	121	15	2	2504	3	10	3690
A424	70	1	97	4	22	33	14	1	11	25	
A452	3		2	124	39	1		45			
A521	13		6	19	29	1	5			2	
A094	9	11	26	1	1	36	65		76	76	
A108	6		6	121	26	4		282		1	81
A643	3		5			6	3			6	
A877	4		12	5	7	9	2	1	4	4	
B192	8		11	95	40	7		62			1
B230	2	1	32			66	12		10	44	
C593	43		50	2	31	37	3		1	14	
C594	6		3	74	28	2		28		1	
C595	30		48	26	39	25		15		4	
B491							5		5	7	
C596	53		50	2	30	37	1		1	4	
B540		14					17		29	22	
C598	17		18	143	42	9		349			62
C294	183	2	304	136	309	182	1	8	1	7	
C821	48	2	58	7	69	53	12	1	6	30	
D012	51		35	238	214	16		44		1	33
D338	16		173			283	7		1	81	
D356	8		10	46	20	7		32		1	
D402	10	1	14			9	1		1	17	
D444	25		20	38	32	2				1	
D537	23		6	211	132	3		26			
D666	8	2	22		1	36	4		3	15	
D839		1	15			43	10		1	24	
E029	39	1	26	125	89	30	6	165	7	25	7
E165	14		17	57	41	20		383		7	343
E167	1	6	2			5	20		32	10	
E168	1	4	4			33	44		42	55	
E273	11	2	76	5	6	118	13	4	5	41	
E306	16		12	49	71	5	1	2	1	2	
E369	3	4	7		1	31	6		11	24	
E371	67	5	65	2	79	35	11		6	15	
E391				10				129			86
A308		1				2	5		15	4	
E458	32		20	162	84	6		173		1	1
E470	7		6	76	53	1		31			
E587	2	1	34			47	2		2	9	

Table A2. *Cont.*

ID Italian VDA Municipality	Cluster ID—Mean Gain LST Max—n° Population Exposed VDA General										
	I	II	III	IV	V	VI	VII	VIII	IX	X	XI
F367	69		55	108	162	15	1	8		2	
F726	8		2	175	36	1		226		1	54
F987	48		34	337	139	21	2	139	3	8	28
G045	5			14	11			2			
G012	7		3	17	16	3				1	
G459			7			49	3			31	
G794	3		1	135	23	1		205			10
G854		1				7	12		1	14	
G545	31		22	36	129	2				1	
G860	231	1	330	40	118	147	5		1	14	
H042	20		9	73	82	2	1	45		2	7
H110	50		44	458	164	21	3	291	1	11	38
H262	4		4		1	6				4	
H263	6		6	4	12	7			1	2	
H497	3			161	23			104			
H669	4		11	173	16	1		525			92
H670	11	3	13	9	13	12	9	2	7	16	
H671	15		18	148	51	6	1	68	1	2	1
H672	8		14	22	22	2	1	1		1	
H673	3		13		1	18	5		3	10	
H674	5	2	5	195	20	7	4	420	4	6	166
H675	6		7	5	8	27		2		8	
H676	171	1	88	195	431	26	7	22	4	18	
I442	41		26	411	83	29	1	567	1	11	147
L217		12	2			8	29		28	34	
L582	7		3	7	14			1			
L643	19		18	46	40	5		20		1	
L647	12		4	4	11	7				4	
L654		20	16			92	84		78	156	
L783	40	1	50	16	47	62	18	2	7	39	
C282	147		122	81	89	56		38		18	7
L981	16		10	102	45	2		123			7
VDA overall	1866	106	2291	5360	3468	1958	475	7095	427	1062	4862
VDA overall %	6.4	0.4	7.9	18.5	12.0	6.8	1.6	24.5	1.5	3.7	16.8

ID Italian VDA Municipality	Cluster ID—Mean Gain LST Max—n° Population Exposed VDA Elderly 60 Plus										
	I	II	III	IV	V	VI	VII	VIII	IX	X	XI
A205	10		19		1	35	3		1	13	
A305	1	3	21			61	18		10	55	
A326	39	1	31	775	143	14	1	4048	2	9	5644
A424	102	1	131	5	26	44	17	1	14	30	
A452	5		5	125	48	2		41		1	
A521	16		8	19	33	3	3	1		2	
A094	8	18	27		1	38	73		106	88	
A108	9		6	130	34	2		306		1	88
A643	5		9			11	6			11	
A877	4		14	6	8	11	3	1	6	4	
B192	8		14	96	38	11		62		1	2
B230	2	2	37			84	17		20	65	
C593	51		69	4	32	54	4		2	24	
C594	13		3	76	47	3		34		1	
C595	46	1	71	35	57	36	1	16		6	
B491		1				1	10		11	11	
C596	48		55	1	23	44	1			5	
B540		19				1	28		40	38	
C598	13		12	138	35	5		333			58
C294	223	1	376	168	381	247		6		5	

Table A2. *Cont.*

ID Italian VDA Municipality	I	II	III	IV	V	VI	VII	VIII	IX	X	XI
				Cluster ID—Mean Gain LST Max—n° Population Exposed VDA General							
C821	80	3	90	15	119	82	21	1	11	49	
D012	57		43	263	254	21		37		1	27
D338	18		231			372	9		1	104	
D356	11		12	71	30	8	1	31		5	
D402	9		16			16	1		1	30	
D444	28		25	43	39	7				2	
D537	29		8	251	161	4		30			
D666	13	3	36		1	63	8		5	28	
D839		3	29			86	9		6	42	
E029	35		23	102	78	26	3	133	3	17	6
E165	9		12	53	30	14		463		5	354
E167	1	4	3			6	20		28	8	
E168	1	4	4			40	59		47	75	
E273	14	2	80	7	8	143	17	5	6	55	
E306	15		12	59	75	5		3		2	
E369	3	6	8		1	45	10		16	38	
E371	104	8	97	3	128	44	10		9	19	
E391				8				101			71
A308		1				3	7		18	6	
E458	42		24	172	104	8		196		1	2
E470	8		7	89	56	1		38			
E587	3	1	54			67	3		3	13	
F367	71		60	105	185	13		8		1	
F726	4		1	200	37	1		242			55
F987	53		39	292	137	29	4	115	7	12	26
G045	7		1	20	14			3			
G012	7		4	13	17	5				1	
G459		2	7			56	14		4	43	
G794	4		1	133	25	1		193		1	10
G854						14	25		1	25	
G545	29		21	34	122	2				2	
G860	288		440	48	147	198	7		2	21	
H042	23		11	79	98	1		43	1	1	6
H110	49	1	49	431	158	26	5	273	4	14	43
H262	3		3		1	8	1			9	
H263	15		6	7	24	5			1	2	
H497	2			149	19			100			
H669	4		10	186	16	1		610			102
H670	12	3	9	7	15	18	9	2	5	19	
H671	20		22	171	58	10		85		3	2
H672	10		10	26	24	3	2	1		2	
H673	4		17		1	24	7		4	13	
H674	4	3	3	206	20	11	4	418	4	4	167
H675	8		11	6	12	41		4		12	1
H676	234		114	265	646	31	5	24	4	20	
I442	44		34	389	87	35	1	565	5	8	165
L217		17	2			9	41		41	50	
L582	11		5	16	29	1		1		1	
L643	25		24	49	47	5		24		1	
L647	14		9	6	14	9		1		3	
L654		20	20			119	87		87	160	
L783	51	2	68	22	64	95	31	2	15	59	
C282	204	1	168	123	150	75	2	44	1	26	11
L981	18		8	116	52	2		130			9

Table A2. *Cont.*

ID Italian VDA Municipality	Cluster ID—Mean Gain LST Max—n° Population Exposed VDA General										
	I	**II**	**III**	**IV**	**V**	**VI**	**VII**	**VIII**	**IX**	**X**	**XI**
VDA overall	2299	135	2901	5816	4210	2613	611	8772	553	1383	6851
VDA overall %	6.4	0.4	8.0	16.1	11.6	7.2	1.7	24.3	1.5	3.8	19.0
ID Italian VDA Municipality	Cluster ID—Mean Gain LST Max—n° Population Exposed Children under 5										
	I	II	III	IV	V	VI	VII	VIII	IX	X	XI
A205	2		6		1	4				3	
A305		2	3			12	5		2	14	
A326	9		10	127	27	3		520	1	2	732
A424	15		20	1	4	6	3		2	6	
A452				29	8			11			
A521	5		3	10	13	1	3			2	
A094	2	5	8			12	15		29	21	
A108	1			27	5			57			16
A643			1			1	1			1	
A877	1		3	1	2	2	1		1	1	
B192	1		2	19	8			13			
B230			10			15	2		3	9	
C593	8		9		8	9				4	
C594	1			15	5	1		6			
C595	7		9	5	9	4		2		1	
B491							1		1	1	
C596	9		9			6	7			1	
B540		1					2		5	3	
C598	4		4	34	10	2		82			14
C294	39	1	70	33	76	32		2		1	
C821	9		11	1	12	9	2		1	4	
D012	9		5	50	44	2		8			8
D338	3		34			66	1			19	
D356	2		2	10	4	2		8			
D402	1		3			4				6	
D444	7		7	6	6	1					
D537	5		2	56	30	1		8			
D666	1		4			9	1		1	4	
D839			2			8	3			4	
E029	8		7	31	21	8	1	45	1	5	2
E165	2		2	11	7	3		87		1	91
E167		2	1			1	7		10	4	
E168		2	1			8	7		9	10	
E273	2	1	7	1	1	17	3	1	1	8	
E306	4		4	16	20	1		1		1	
E369	1	1	2			10	2		4	6	
E371	17	2	17		19	8	3		2	4	
E391				2				28			20
A308						1	1		3	1	
E458	11		7	41	23	1		49			
E470	1		1	16	10			7			
E587			5			7	1		1	2	
F367	12		12	23	35	3		2			
F726	3		1	39	9			48			10
F987	12		8	76	31	3	1	31	1	1	7
G045	1			2	2						
G012	2		1	5	5					1	
G459			1			8	1			7	
G794	1			27	4			48			2
G854						3				4	
G545	4		3	4	20						
G860	50		69	8	24	31	1			1	

Table A2. *Cont.*

ID Italian VDA Municipality	Cluster ID—Mean Gain LST Max—n° Population Exposed VDA General										
	I	II	III	IV	V	VI	VII	VIII	IX	X	XI
H042	5		2	16	18	1		9		1	1
H110	12		10	114	40	5	1	70		2	9
H262	1		1			3				3	
H263	1		2	1	2	2				1	
H497	1			35	6			21			
H669	1		3	45	4			122			18
H670	2		4	2	3	3	2		1	4	
H671	3		6	31	13	1	1	15		1	
H672	3		3	4	4	1					
H673	1		2			3	1			2	
H674	1	1	2	42	5	1	2	95	2	2	45
H675	1		1	2	2	4		1		1	
H676	30		17	29	76	4	3	4		4	
I442	10		8	85	19	8		114		3	33
L217		3				1	7		6	7	
L582				1	2						
L643	6		5	11	11	1		5			
L647	2		1		2	2				2	
L654		4	4			21	19		19	33	
L783	15	1	17	4	18	17	4		3	8	
C282	39		31	16	18	13		7		5	1
L981	2		1	21	9			33			3
VDA overall	409	30	504	1190	760	420	110	1562	114	241	1013
VDA overall %	6.4	0.5	7.9	18.7	12.0	6.6	1.7	24.6	1.8	3.8	15.9

ID Italian VDA Municipality	Cluster ID—Mean Gain LST Max—n° Population Exposed VDA Youth 15–24										
	I	II	III	IV	V	VI	VII	VIII	IX	X	XI
A205	3		3		2	3				1	
A305		2	5			20	5		3	16	
A326	17		15	262	56	7	1	1044	2	6	1493
A424	26		39	2	10	16	6		5	11	
A452	1			53	19			17			
A521	4		2	9	9		1				
A094	4	3	10			12	34		32	34	
A108	2		1	39	8			97			28
A643	1		2			2	1			2	
A877	1		6	1	2	4				1	
B192	3		5	37	15	5		24			1
B230	1	1	14			26	6		6	18	
C593	23		23	1	15	17	1			4	
C594	2		1	27	10			10			
C595	13		19	15	20	8		9		1	
B491							2		2	3	
C596	19		20	1	9	14				1	
B540		6					9		13	14	
C598	7		7	57	18	4		136			29
C294	76	1	126	58	127	82		4		2	
C821	18	1	21	3	26	19	5		2	9	
D012	23		16	100	88	6		19			14
D338	7		65			112	3			35	
D356	3		5	19	9	3		12			
D402	1		3			2				7	
D444	9		8	14	13	2					
D537	8		2	69	46	1		10			
D666	3	1	10			12	2		2	6	
D839			6			15	3			10	
E029	17		11	42	34	11	2	53	2	8	2

Table A2. *Cont.*

ID Italian VDA Municipality	I	II	III	IV	V	VI	VII	VIII	IX	X	XI
E165	4		6	19	12	6		140		2	119
E167	1	2	2			4	7		9	6	
E168		2	1			12	19		20	22	
E273	4	1	31	2	3	46	5	2	2	16	
E306	8		5	21	35	3				1	
E369	1	1	2			13	2		3	11	
E371	27	1	24	1	34	15	4		2	5	
E391				4				54			34
A308						1	2		6	2	
E458	12		7	57	29	2		67			1
E470	4		3	37	28			15			
E587	1		15			18	1			3	
F367	28		22	41	60	5		3			
F726	2		1	67	13			86			22
F987	20		15	132	57	8		56		3	11
G045	2			2	3						
G012	1			6	8						
G459			2			16	1			13	
G794	2			63	11			89			5
G854						2	10		1	6	
G545	14		11	18	55	1				1	
G860	93		141	15	47	60	3		1	7	
H042	7		3	31	34	1		17			2
H110	20		17	168	65	6	1	112		3	15
H262	2		2		1	3				2	
H263	2		4	2	4	4				1	
H497	1			70	9			45			
H669	2		5	63	7			177			26
H670	5	1	4	4	7	4	1	1	1	3	
H671	8		9	56	21	2		25		1	
H672	2		8	8	8	1	1				
H673	1		6			9	3		1	5	
H674	2	1	2	77	7	4	2	155	2	2	52
H675	2		3	1	3	12				4	
H676	69		33	80	172	10	2	10		4	
I442	18		10	156	36	10	1	230		3	59
L217		3	2			4	10		11	13	
L582	3		1	5	6			1			
L643	10		9	20	19	3		9		1	
L647	3		1	1	4	1				1	
L654		8	6			34	34		35	62	
L783	10		13	4	13	17	5	1	2	14	
C282	61		50	37	42	20		17		7	3
L981	9		6	48	21	1		51			2
VDA overall	753	39	926	2122	1408	767	196	2799	168	417	1918
VDA overall %	6.5	0.3	8.0	18.4	12.2	6.7	1.7	24.3	1.5	3.6	16.7

Note: The header spans "Cluster ID—Mean Gain LST Max—n° Population Exposed VDA General" over columns I–XI.

References

1. Xu, Z.; Cheng, J.; Hu, W.; Tong, S. Heatwave and Health Events: A Systematic Evaluation of Different Temperature Indicators, Heatwave Intensities and Durations. *Sci. Total Environ.* **2018**, *630*, 679–689. [CrossRef] [PubMed]
2. Ganguly, A.R.; Steinhaeuser, K.; Erickson, D.J., III; Branstetter, M.; Parish, E.S.; Singh, N.; Drake, J.B.; Buja, L. Higher Trends but Larger Uncertainty and Geographic Variability in 21st Century Temperature and Heat Waves. *Proc. Natl. Acad. Sci. USA* **2009**, *106*, 15555–15559. [CrossRef] [PubMed]
3. Orusa, T.; Borgogno Mondino, E. Exploring Short-Term Climate Change Effects on Rangelands and Broad-Leaved Forests by Free Satellite Data in Aosta Valley (Northwest Italy). *Climate* **2021**, *9*, 47. [CrossRef]

4. Heaviside, C.; Vardoulakis, S.; Cai, X.-M. Attribution of Mortality to the Urban Heat Island during Heatwaves in the West Midlands, UK. *Environ. Health* **2016**, *15*, 49–59. [CrossRef]

5. Lemonsu, A.; Viguie, V.; Daniel, M.; Masson, V. Vulnerability to Heat Waves: Impact of Urban Expansion Scenarios on Urban Heat Island and Heat Stress in Paris (France). *Urban Clim.* **2015**, *14*, 586–605. [CrossRef]

6. Li, Y.; Zhang, H.; Kainz, W. Monitoring Patterns of Urban Heat Islands of the Fast-Growing Shanghai Metropolis, China: Using Time-Series of Landsat TM/ETM+ Data. *Int. J. Appl. Earth Obs. Geoinf.* **2012**, *19*, 127–138. [CrossRef]

7. Ma, S.; Pitman, A.; Hart, M.; Evans, J.P.; Haghdadi, N.; MacGill, I. The Impact of an Urban Canopy and Anthropogenic Heat Fluxes on Sydney's Climate. *Int. J. Climatol.* **2017**, *37*, 255–270. [CrossRef]

8. Orusa, T.; Mondino, E.B. Landsat 8 Thermal Data to Support Urban Management and Planning in the Climate Change Era: A Case Study in Torino Area, NW Italy. In *Remote Sensing Technologies and Applications in Urban Environments IV, Proceedings of the SPIE, Strasbourg, France, 9–10 September 2019*; International Society for Optics and Photonics: Bellingham, WA, USA, 2019; Volume 11157, pp. 133–149.

9. Dewan, A.; Kiselev, G.; Botje, D.; Mahmud, G.I.; Bhuian, M.H.; Hassan, Q.K. Surface Urban Heat Island Intensity in Five Major Cities of Bangladesh: Patterns, Drivers and Trends. *Sustain. Cities Soc.* **2021**, *71*, 102926. [CrossRef]

10. QGIS Development Team. *QGIS Geographic Information System*; Open Source Geospatial Foundation Project: Beaverton, OR, USA, 2018.

11. Nakhapakorn, K.; Sancharoen, W.; Mutchimwong, A.; Jirakajohnkool, S.; Onchang, R.; Rotejanaprasert, C.; Tantrakarnapa, K.; Paul, R. Assessment of Urban Land Surface Temperature and Vertical City Associated with Dengue Incidences. *Remote Sens.* **2020**, *12*, 3802. [CrossRef]

12. Al-Hameedi, W.M.M.; Chen, J.; Faichia, C.; Nath, B.; Al-Shaibah, B.; Al-Aizari, A. Geospatial Analysis of Land Use/Cover Change and Land Surface Temperature for Landscape Risk Pattern Change Evaluation of Baghdad City, Iraq, Using CA–Markov and ANN Models. *Sustainability* **2022**, *14*, 8568. [CrossRef]

13. Ward, K.; Lauf, S.; Kleinschmit, B.; Endlicher, W. Heat Waves and Urban Heat Islands in Europe: A Review of Relevant Drivers. *Sci. Total Environ.* **2016**, *569*, 527–539. [CrossRef] [PubMed]

14. Ramamurthy, P.; Bou-Zeid, E. Heatwaves and Urban Heat Islands: A Comparative Analysis of Multiple Cities. *J. Geophys. Res. Atmos.* **2017**, *122*, 168–178. [CrossRef]

15. Bagliani, M.M.; Caimotto, M.C.; Latini, G.; Orusa, T. *Lessico e Nuvole: Le Parole Del Cambiamento Climatico*; University of Turin: Turin, Italy, 2019.

16. Kafy, A.-A.; Shuvo, R.M.; Naim, M.N.H.; Sikdar, M.S.; Chowdhury, R.R.; Islam, M.A.; Sarker, M.H.S.; Khan, M.H.H.; Kona, M.A. Remote Sensing Approach to Simulate the Land Use/Land Cover and Seasonal Land Surface Temperature Change Using Machine Learning Algorithms in a Fastest-Growing Megacity of Bangladesh. *Remote Sens. Appl. Soc. Environ.* **2021**, *21*, 100463. [CrossRef]

17. Fu, X.; Yao, L.; Sun, S. Accessing the Heat Exposure Risk in Beijing–Tianjin–Hebei Region Based on Heat Island Footprint Analysis. *Atmosphere* **2022**, *13*, 739. [CrossRef]

18. Begum, M.S.; Bala, S.K.; Islam, A.S.; Islam, G.T.; Roy, D. An Analysis of Spatio-Temporal Trends of Land Surface Temperature in the Dhaka Metropolitan Area by Applying Landsat Images. *J. Geogr. Inf. Syst.* **2021**, *13*, 538–560. [CrossRef]

19. Carella, E.; Orusa, T.; Viani, A.; Meloni, D.; Borgogno-Mondino, E.; Orusa, R. An Integrated, Tentative Remote-Sensing Approach Based on NDVI Entropy to Model Canine Distemper Virus in Wildlife and to Prompt Science-Based Management Policies. *Animals* **2022**, *12*, 1049. [CrossRef]

20. Orusa, T.; Orusa, R.; Viani, A.; Carella, E.; Borgogno Mondino, E. Geomatics and EO Data to Support Wildlife Diseases Assessment at Landscape Level: A Pilot Experience to Map Infectious Keratoconjunctivitis in Chamois and Phenological Trends in Aosta Valley (NW Italy). *Remote Sens.* **2020**, *12*, 3542. [CrossRef]

21. Pourghasemi, H.R.; Pouyan, S.; Heidari, B.; Farajzadeh, Z.; Shamsi, S.R.F.; Babaei, S.; Khosravi, R.; Etemadi, M.; Ghanbarian, G.; Farhadi, A.; et al. Spatial Modeling, Risk Mapping, Change Detection, and Outbreak Trend Analysis of Coronavirus (COVID-19) in Iran (Days between February 19 and June 14, 2020). *Int. J. Infect. Dis.* **2020**, *98*, 90–108. [CrossRef]

22. Squadrone, S.; Brizio, P.; Stella, C.; Mantia, M.; Battuello, M.; Nurra, N.; Sartor, R.M.; Orusa, R.; Robetto, S.; Brusa, F.; et al. Rare Earth Elements in Marine and Terrestrial Matrices of Northwestern Italy: Implications for Food Safety and Human Health. *Sci. Total Environ.* **2019**, *660*, 1383–1391. [CrossRef]

23. Kestens, Y.; Brand, A.; Fournier, M.; Goudreau, S.; Kosatsky, T.; Maloley, M.; Smargiassi, A. Modelling the Variation of Land Surface Temperature as Determinant of Risk of Heat-Related Health Events. *Int. J. Health Geogr.* **2011**, *10*, 7. [CrossRef]

24. De Marinis, P.; De Petris, S.; Sarvia, F.; Manfron, G.; Momo, E.J.; Orusa, T.; Corvino, G.; Sali, G.; Borgogno, E.M. Supporting Pro-Poor Reforms of Agricultural Systems in Eastern DRC (Africa) with Remotely Sensed Data: A Possible Contribution of Spatial Entropy to Interpret Land Management Practices. *Land* **2021**, *10*, 1368. [CrossRef]

25. Malakar, N.K.; Hulley, G.C.; Hook, S.J.; Laraby, K.; Cook, M.; Schott, J.R. An Operational Land Surface Temperature Product for Landsat Thermal Data: Methodology and Validation. *IEEE Trans. Geosci. Remote Sens.* **2018**, *56*, 5717–5735. [CrossRef]

26. Masek, J.G. *Landsat Ecosystem Disturbance Adaptive Processing System (LEDAPS)*; U.S. Geological Survey: Reston, VA, USA, 2006.

27. Fisher, J.B.; Lee, B.; Purdy, A.J.; Halverson, G.H.; Dohlen, M.B.; Cawse-Nicholson, K.; Wang, A.; Anderson, R.G.; Aragon, B.; Arain, M.A.; et al. ECOSTRESS: NASA's next Generation Mission to Measure Evapotranspiration from the International Space Station. *Water Resour. Res.* **2020**, *56*, e2019WR026058. [CrossRef]

28. Hulley, G.C.; Göttsche, F.M.; Rivera, G.; Hook, S.J.; Freepartner, R.J.; Martin, M.A.; Cawse-Nicholson, K.; Johnson, W.R. Validation and Quality Assessment of the ECOSTRESS Level-2 Land Surface Temperature and Emissivity Product. *IEEE Trans. Geosci. Remote Sens.* **2021**, *60*, 21518764. [CrossRef]

29. Halverson, G.H.; Fisher, J.B.; Lee, C.M. *ECOsystem Spaceborne Thermal Radiometer Experiment on Space Station (ECOSTRESS) Mission*; NASA: Washington, DC, USA, 2019.

30. Hulley, G.; Shivers, S.; Wetherley, E.; Cudd, R. New ECOSTRESS and MODIS Land Surface Temperature Data Reveal Fine-Scale Heat Vulnerability in Cities: A Case Study for Los Angeles County, California. *Remote Sens.* **2019**, *11*, 2136. [CrossRef]

31. Meerdink, S.K.; Hook, S.J.; Roberts, D.A.; Abbott, E.A. The ECOSTRESS Spectral Library Version 1.0. *Remote Sens. Environ.* **2019**, *230*, 111196. [CrossRef]

32. Yelamanchili, A.; Chien, S.; Cawse-Nicholson, K.; Freeborn, D.; Padams, J. *Scheduling and Operations of the ECOSTRESS Mission*; NASA: Washington, DC, USA, 2021.

33. Ermida, S. *Harmonization of Remote Sensing Land Surface Products: Correction of Clear-Sky Bias and Characterization of Directional Effects*; Repositório da Universidade de Lisboa: Lisbon, Portugal, 2018.

34. Ermida, S.L.; Trigo, I.F.; DaCamara, C.C.; Roujean, J.-L. Assessing the Potential of Parametric Models to Correct Directional Effects on Local to Global Remotely Sensed LST. *Remote Sens. Environ.* **2018**, *209*, 410–422. [CrossRef]

35. Ermida, S.L.; Trigo, I.F.; DaCamara, C.C.; Jiménez, C.; Prigent, C. Quantifying the Clear-Sky Bias of Satellite Land Surface Temperature Using Microwave-Based Estimates. *J. Geophys. Res. Atmos.* **2019**, *124*, 844–857. [CrossRef]

36. Ermida, S.L.; Soares, P.; Mantas, V.; Göttsche, F.-M.; Trigo, I.F. Google Earth Engine Open-Source Code for Land Surface Temperature Estimation from the Landsat Series. *Remote Sens.* **2020**, *12*, 1471. [CrossRef]

37. Fassnacht, F.E.; Li, L.; Fritz, A. Mapping Degraded Grassland on the Eastern Tibetan Plateau with Multi-Temporal Landsat 8 Data—Where Do the Severely Degraded Areas Occur? *Int. J. Appl. Earth Obs. Geoinf.* **2015**, *42*, 115–127. [CrossRef]

38. Fu, P.; Weng, Q. A Time Series Analysis of Urbanization Induced Land Use and Land Cover Change and Its Impact on Land Surface Temperature with Landsat Imagery. *Remote Sens. Environ.* **2016**, *175*, 205–214. [CrossRef]

39. Kumar, D.; Shekhar, S. Statistical Analysis of Land Surface Temperature–Vegetation Indexes Relationship through Thermal Remote Sensing. *Ecotoxicol. Environ. Saf.* **2015**, *121*, 39–44. [CrossRef] [PubMed]

40. Lee, P.S.-H.; Park, J. An Effect of Urban Forest on Urban Thermal Environment in Seoul, South Korea, Based on Landsat Imagery Analysis. *Forests* **2020**, *11*, 630. [CrossRef]

41. Goward, S.N. Thermal Behavior of Urban Landscapes and the Urban Heat Island. *Phys. Geogr.* **1981**, *2*, 19–33. [CrossRef]

42. Founda, D.; Santamouris, M. Synergies between Urban Heat Island and Heat Waves in Athens (Greece), during an Extremely Hot Summer (2012). *Sci. Rep.* **2017**, *7*, 10973. [CrossRef]

43. Gorelick, N.; Hancher, M.; Dixon, M.; Ilyushchenko, S.; Thau, D.; Moore, R. Google Earth Engine: Planetary-Scale Geospatial Analysis for Everyone. *Remote Sens. Environ.* **2017**, *202*, 18–27. [CrossRef]

44. Batista e Silva, F.; Gallego, J.; Lavalle, C. A High-Resolution Population Grid Map for Europe. *J. Maps* **2013**, *9*, 16–28. [CrossRef]

45. Huang, X.; Wang, C.; Li, Z.; Ning, H. A 100 m Population Grid in the CONUS by Disaggregating Census Data with Open-Source Microsoft Building Footprints. *Big Earth Data* **2021**, *5*, 112–133. [CrossRef]

46. Patel, N.N.; Angiuli, E.; Gamba, P.; Gaughan, A.; Lisini, G.; Stevens, F.R.; Tatem, A.J.; Trianni, G. Multitemporal Settlement and Population Mapping from Landsat Using Google Earth Engine. *Int. J. Appl. Earth Obs. Geoinf.* **2015**, *35*, 199–208. [CrossRef]

47. Reed, F.J.; Gaughan, A.E.; Stevens, F.R.; Yetman, G.; Sorichetta, A.; Tatem, A.J. Gridded Population Maps Informed by Different Built Settlement Products. *Data* **2018**, *3*, 33. [CrossRef]

48. Verhulst, S.; Ramesh, A.; Young, A.; Zahuranec, A.J. *Where Is Everyone? The Importance of Population Density Data: A Data Artefact Study of the Facebook Population Density Map (September 21, 2021)*; Elsevier: Amsterdam, The Netherlands, 2021.

49. Wang, X.; Meng, X.; Long, Y. Projecting 1 Km-Grid Population Distributions from 2020 to 2100 Globally under Shared Socioeconomic Pathways. *Sci. Data* **2022**, *9*, 563. [CrossRef] [PubMed]

50. Tiecke, T.G.; Liu, X.; Zhang, A.; Gros, A.; Li, N.; Yetman, G.; Kilic, T.; Murray, S.; Blankespoor, B.; Prydz, E.B.; et al. Mapping the World Population One Building at a Time. *arXiv* **2017**, arXiv:1712.05839.

51. Esch, T.; Heldens, W.; Hirner, A.; Keil, M.; Marconcini, M.; Roth, A.; Zeidler, J.; Dech, S.; Strano, E. Breaking New Ground in Mapping Human Settlements from Space—The Global Urban Footprint. *ISPRS J. Photogramm. Remote Sens.* **2017**, *134*, 30–42. [CrossRef]

52. Esch, T.; Schenk, A.; Ullmann, T.; Thiel, M.; Roth, A.; Dech, S. Characterization of Land Cover Types in TerraSAR-X Images by Combined Analysis of Speckle Statistics and Intensity Information. *IEEE Trans. Geosci. Remote Sens.* **2011**, *49*, 1911–1925. [CrossRef]

53. Potere, D.; Schneider, A.; Angel, S.; Civco, D.L. Mapping Urban Areas on a Global Scale: Which of the Eight Maps Now Available Is More Accurate? *Int. J. Remote Sens.* **2009**, *30*, 6531–6558. [CrossRef]

54. Pesaresi, M.; Huadong, G.; Blaes, X.; Ehrlich, D.; Ferri, S.; Gueguen, L.; Halkia, M.; Kauffmann, M.; Kemper, T.; Lu, L.; et al. A Global Human Settlement Layer from Optical HR/VHR RS Data: Concept and First Results. *IEEE J. Sel. Top. Appl. Earth Obs. Remote Sens.* **2013**, *6*, 2102–2131. [CrossRef]

55. Felbier, A.; Esch, T.; Heldens, W.; Marconcini, M.; Zeidler, J.; Roth, A.; Klotz, M.; Wurm, M.; Taubenböck, H. The Global Urban Footprint—Processing Status and Cross Comparison to Existing Human Settlement Products. In Proceedings of the 2014 IEEE Geoscience and Remote Sensing Symposium, Quebec City, QC, Canada, 13–18 July 2014; pp. 4816–4819.

56. Linard, C.; Tatem, A.; Stevens, F.R.; Gaughan, A.; Patel, N.N.; Huang, Z. Use of Active and Passive VGI Data for Population Distribution Modelling: Experience from the WorldPop Project. In Proceedings of the Eighth International Conference on Geographic Information Science, Vienna, Austria, 24–26 September 2014.

57. Bright, E.A.; Rose, A.N.; Urban, M.L.; McKee, J. *LandScan 2017 High-Resolution Global Population Data Set*; Oak Ridge National Lab (ORNL): Oak Ridge, TN, USA, 2018.

58. Bhaduri, B.; Bright, E.; Coleman, P.; Dobson, J. LandScan. *Geoinformatics* **2002**, *5*, 34–37.

59. Givoni, M. Between Micro Mappers and Missing Maps: Digital Humanitarianism and the Politics of Material Participation in Disaster Response. *Environ. Plan. D Soc. Space* **2016**, *34*, 1025–1043. [CrossRef]

60. Holloway, J.; Helmstedt, K.J.; Mengersen, K.; Schmidt, M. A Decision Tree Approach for Spatially Interpolating Missing Land Cover Data and Classifying Satellite Images. *Remote Sens.* **2019**, *11*, 1796. [CrossRef]

61. Warszawski, L.; Frieler, K.; Huber, V.; Piontek, F.; Serdeczny, O.; Zhang, X.; Tang, Q.; Pan, M.; Tang, Y.; Tang, Q.; et al. Center for International Earth Science Information Network—CIESIN—Columbia University.(2016). Gridded Population of the World, Version 4 (GPWv4): Population Density. Palisades. NY: NASA Socioeconomic Data and Applications Center (SEDAC). In *Atlas of Environmental Risks Facing China Under Climate Change*; Springer: Berlin/Heidelberg, Germany, 2017; p. 228. [CrossRef]

62. Samuele, D.P.; Filippo, S.; Orusa, T.; Enrico, B.-M. Mapping SAR Geometric Distortions and Their Stability along Time: A New Tool in Google Earth Engine Based on Sentinel-1 Image Time Series. *Int. J. Remote Sens.* **2021**, *42*, 9135–9154. [CrossRef]

63. Sekertekin, A.; Bonafoni, S. Land Surface Temperature Retrieval from Landsat 5, 7, and 8 over Rural Areas: Assessment of Different Retrieval Algorithms and Emissivity Models and Toolbox Implementation. *Remote Sens.* **2020**, *12*, 294. [CrossRef]

64. Rubio, E.; Caselles, V.; Badenas, C. Emissivity Measurements of Several Soils and Vegetation Types in the 8–14, Mm Wave Band: Analysis of Two Field Methods. *Remote Sens. Environ.* **1997**, *59*, 490–521. [CrossRef]

65. Cristóbal, J.; Jiménez-Muñoz, J.; Sobrino, J.; Ninyerola, M.; Pons, X. Improvements in Land Surface Temperature Retrieval from the Landsat Series Thermal Band Using Water Vapor and Air Temperature. *J. Geophys. Res. Atmos.* **2009**, 114. [CrossRef]

66. Carlson, T.N.; Ripley, D.A. On the Relation between NDVI, Fractional Vegetation Cover, and Leaf Area Index. *Remote Sens. Environ.* **1997**, *62*, 241–252. [CrossRef]

67. Kauth, R.J.; Thomas, G. The Tasselled Cap—A Graphic Description of the Spectral-Temporal Development of Agricultural Crops as Seen by Landsat. In Proceedings of the LARS Symposium on Machine Processing of Remotely Sensed Data, West Lafayette, IN, USA, 29 June–1 July 1976; p. 159.

68. Orusa, T.; Viani, A.; Cammareri, D.; Borgogno Mondino, E. A Google Earth Engine Algorithm to Map Phenological Metrics in Mountain Areas Worldwide with Landsat Collection and Sentinel-2. *Geomatics* **2023**, *3*, 221–238. [CrossRef]

69. Roy, D.P.; Zhang, H.; Ju, J.; Gomez-Dans, J.L.; Lewis, P.E.; Schaaf, C.; Sun, Q.; Li, J.; Huang, H.; Kovalskyy, V. A General Method to Normalize Landsat Reflectance Data to Nadir BRDF Adjusted Reflectance. *Remote Sens. Environ.* **2016**, *176*, 255–271. [CrossRef]

70. Schafer, R.W. What Is a Savitzky-Golay Filter? [Lecture Notes]. *IEEE Signal Process. Mag.* **2011**, *28*, 111–117. [CrossRef]

71. Chen, J.; Jönsson, P.; Tamura, M.; Gu, Z.; Matsushita, B.; Eklundh, L. A Simple Method for Reconstructing a High-Quality NDVI Time-Series Data Set Based on the Savitzky–Golay Filter. *Remote Sens. Environ.* **2004**, *91*, 332–344. [CrossRef]

72. Press, W.H.; Teukolsky, S.A. Savitzky-Golay Smoothing Filters. *Comput. Phys.* **1990**, *4*, 669–672. [CrossRef]

73. Conrad, O.; Bechtel, B.; Bock, M.; Dietrich, H.; Fischer, E.; Gerlitz, L.; Wehberg, J.; Wichmann, V.; Böhner, J. System for Automated Geoscientific Analyses (SAGA) v. 2.1.4. *Geosci. Model Dev.* **2015**, *8*, 1991–2007. [CrossRef]

74. Orusa, T.; Cammareri, D.; Borgogno Mondino, E. A Scalable Earth Observation Service to Map Land Cover in Geomorphological Complex Areas beyond the Dynamic World: An Application in Aosta Valley (NW Italy). *Appl. Sci.* **2022**, *13*, 390. [CrossRef]

75. Orusa, T.; Cammareri, D.; Borgogno Mondino, E. A Possible Land Cover EAGLE Approach to Overcome Remote Sensing Limitations in the Alps Based on Sentinel-1 and Sentinel-2: The Case of Aosta Valley (NW Italy). *Remote Sens.* **2022**, *15*, 178. [CrossRef]

76. Sarvia, F.; Petris, S.D.; Orusa, T.; Borgogno-Mondino, E. MAIA S2 Versus Sentinel 2: Spectral Issues and Their Effects in the Precision Farming Context. In *Computational Science and Its Applications—ICCSA 2021, Proceedings of the 21st International Conference, Cagliari, Italy, 13–16 September 2021*; Springer: Berlin/Heidelberg, Germany, 2021; pp. 63–77.

77. Latini, G.; Bagliani, M.; Orusa, T. *Lessico e Nuvole: Le Parole Del Cambiamento Climatico*; Universita di Torino: Torino, Italy, 2021.

78. Caimotto, M.C.; Fargione, D.; Furiassi, C.G.; Orusa, T.; Alex, P. Parlare è Pensare. In *Lessico e Nuvole: Le Parole del Cambiamento Climatico*, 2nd ed.; Università degli Studi di Torino: Torino, Italy, 2020; pp. 281–284.

79. Tartaglino, A.; Orusa, T. Bilancio Energetico/Energy Balance in Lessico e Nuvole: Le Parole Del Cambiamento Climatico, 2nd ed. In *Bilancio Energetico*; Università degli Studi di Torino: Torino, Italy, 2020; pp. 61–63.

80. Viani, A.; Orusa, T.; Borgogno-Mondino, E.; Orusa, R. Snow Metrics as Proxy to Assess Sarcoptic Mange in Wild Boar: Preliminary Results in Aosta Valley (Italy). *Life* **2023**, *13*, 987. [CrossRef] [PubMed]